Journal of Materials Chemistry B

ROYAL SOCIETY OF CHEMISTRY

PAPER

View Article Online
View Journal

Cite this: DOI: 10.1039/d5tb01738f

Cold plasma triggered cell death with a curcumin and capecitabine loaded magnetic nanocluster-based multifunctional system on the MCF-7 cell line: a smart therapy platform

Demet Erdag, *[abc] M. Dolores Garrido, [bd] Harun Basoglu, [eg] Idris Yazgan, [bf] Pedro Amorós, [d] Leman Yalcintepe[a] and Muhammet S. Toprak †*[b]

The development of smart, selective, and multifunctional nanotherapeutics is crucial for advancing next-generation cancer treatments. In this study, superparamagnetic iron oxide nanoclusters (SPIONCs) were coated with mesoporous silica, functionalized with folic acid (FA), and co-loaded with curcumin (CUR) and capecitabine (CAPE) to create a novel nanocarrier system. To enhance cellular internalisation, magnetophoresis was applied before exposure of the cells to cold atmospheric plasma (CAP). The resulting FA-conjugated, CUR and CAPE-loaded nanoclusters were evaluated *in vitro* in MCF-7 breast cancer and HME-1 normal epithelial cells at varying CAP exposure durations (0, 10, and 20 s) and incubation times (24 and 48 h). This is the first report demonstrating the co-loading of CUR and CAPE into FA-functionalised mesoporous silica-coated magnetic nanoclusters. Drug release studies revealed significantly enhanced release profiles under acidic conditions (pH 5.0 and 6.5), mimicking lysosomal and tumour microenvironments, compared to physiological pH (7.4). Drug-loaded nanoclusters exhibited substantially higher cytotoxicity than the controls with no loading, with a more pronounced effect in MCF-7 cells. Notably, the combined treatment of CAP and CUR-CAPE loaded NCs showed a synergistic cytotoxic effect. IC_{50} values, after 10 s CAP exposure and 24 h incubation, decreased to 0.43 μg mL^{-1} for MCF-7 cells and 37 μg mL^{-1} for HME-1 cells. The elevated levels of reactive oxygen species (ROS) induced by CAP played a key role in the observed cytotoxic effects, and both CUR and CAPE were found to enhance this process through ROS-related and potentially additional molecular pathways. These findings highlight the potential of CAP-assisted multicomponent nanocarriers as a promising platform for effective cancer therapy.

Received 28th July 2025,
Accepted 5th December 2025

DOI: 10.1039/d5tb01738f

rsc.li/materials-b

Introduction

Breast cancer remains the most prevalent malignancy among women worldwide and ranked as the second leading cause of cancer-related mortality in 2023.[1] Despite significant advancements in conventional therapies, challenges such as systemic toxicity, drug resistance, and poor tumour selectivity necessitate innovative treatment strategies.[2] In recent years, magnetic nanoparticles (MNPs) have emerged as a promising class of nanomaterials with broad biomedical applications, including targeted drug delivery, hyperthermia, photodynamic therapy, and magnetic resonance imaging (MRI) contrast enhancement.[3,4] The controlled design of these nanoparticles (NPs) through tailoring their size, surface chemistry, crystallinity, and magnetic properties plays a critical role in optimizing their biomedical functionality.[5,6]

NP-based drug delivery systems offer enhanced therapeutic efficacy by improving bioavailability, extending the circulation time, and enabling tumour-targeted accumulation.[7,8] MNPs can facilitate drug transport through either direct conjugation with anticancer agents or *via* corona-mediated interactions, thus enhancing localized drug retention and minimizing off-target cytotoxicity.[9] However, individual MNPs tend to aggregate under physiological conditions and may dissolve, compromising their

[a] Department of Biophysics, Istanbul University-Faculty of Medicine, Istanbul, Türkiye. E-mail: derdag@kth.se, erdagdem@gmail.com
[b] Department of Applied Physics, KTH Royal Institute of Technology, Stockholm, Sweden. E-mail: toprak@kth.se
[c] Department of Computer Programming, Vocational School, Biruni University, Istanbul, Turkiye
[d] Institut de Ciència dels Materials (ICMUV), Universitat de València, Valencia, Spain
[e] Department of Biophysics, Faculty of Medicine, Karadeniz Technical University, Trabzon, Türkiye
[f] Department of Biology, Faculty of Science, Kastamonu University, Kastamonu, Türkiye
[g] Department of Biophysics, Faculty of Medicine, Bilecik Seyh Edebali University, Bilecik, Türkiye
† Visiting Professor, Department of Physics, National University of Singapore, Singapore.

stability and therapeutic efficacy.[10,11] Most of the existing studies have focused on modifying the surface properties and composition of iron oxide NPs to enhance their magnetic and biological functionalities. While significant efforts have been made to control the shape and size of MNPs, ranging from spherical to cubic and rod-like structures to achieve magnetic anisotropy, there remains a need to explore alternative approaches, such as mesoporous silica coating, to improve drug-loading capacity and targeted therapeutic applications.

To improve tumour specificity, surface modifications with molecular targeting ligands such as antibodies, peptides, and folic acid (FA) have been explored. FA, in particular, is widely used due to its ability to selectively bind folate receptor alpha (FRα), which is overexpressed in various malignancies, including breast cancer.[12] Notably, FRα expression is significantly elevated in HER2-positive breast cancer (SK-BR-3) compared to estrogen receptor-positive (MCF-7) cells, indicating its potential as a selective therapeutic target.[13,14] FA-modified NPs offer enhanced tumour selectivity, controlled drug release, and reduced systemic toxicity, making them a promising strategy for breast cancer therapy.[15] Curcumin (CUR) is a naturally occurring polyphenol with potent antitumor properties known to regulate multiple cellular pathways involved in proliferation and apoptosis. In breast cancer cells, CUR causes oxidative stress by increasing intracellular reactive oxygen species (ROS), contributing to mitochondrial dysfunction, caspase activation, and subsequent apoptotic cell death. It also arrests the cell cycle at the **G2**/M phase by upregulating P21 expression while downregulating CDC25 and CDC2. Furthermore, CUR inhibits the PI3K/Akt/mTOR signalling axis, further enhancing its pro-apoptotic and anti-proliferative effects.[16,17] Capecitabine (CAPE), a widely used prodrug of 5-fluorouracil (5-FU), exhibits preferential tumour activation, minimizing systemic toxicity. It has been extensively employed in the treatment of metastatic breast cancer, offering a more targeted and effective chemotherapeutic approach.[18,19]

Recently, cold atmospheric plasma (CAP) has emerged as a novel cancer therapy due to its ability to generate reactive oxygen and nitrogen species (ROS/RNS), leading to selective tumour cell apoptosis.[20,21] CAP treatment disrupts cellular redox balance and enhances membrane permeability, facilitating improved drug penetration and synergistic therapeutic effects.[22,23] Given its ability to induce electroporation-like effects, CAP holds potential in combination therapies to overcome drug resistance.[24]

We have earlier investigated amorphous and mesoporous silica-coated SPION clusters and characterized them in detail.[10,25] Optimizing the NP size is crucial, as larger particles (>300 nm) may exhibit limited tumour penetration and rapid clearance by the reticuloendothelial system (RES), whereas smaller particles (100–300 nm) can effectively exploit the enhanced permeability and retention (EPR) effect, facilitating selective accumulation in tumour tissues. To address these challenges, this study focuses on the synthesis and characterization of mesoporous silica-coated SPION clusters with optimized size and surface properties, potentially enabling high drug-loading capacity, chemical stability, and controlled release.

Although numerous studies have investigated the superparamagnetic properties of MNPs, limited research has been conducted on the integration of mesoporous silica-coated superparamagnetic iron oxide NPs (SPIONs) for combined drug delivery and cold atmospheric plasma (CAP)-assisted cancer therapy. In this work, SPION-based nanoclusters (SPIONCs) were synthesized and coated with mesoporous silica using the atrane method,[26] designed to achieve structural stability, biocompatibility, and controlled surface functionalization. The synthesized NCs were extensively characterized for their structural, compositional, and magnetic properties. Several active species (Ca^{2+} ions, FA, CUR, and CAPE) have been integrated onto SPIONCs. The drug-loading efficiency, cytotoxicity, and reactive oxygen species (ROS) generation under CAP treatment were systematically evaluated to assess their potential for breast cancer therapy. To determine their selectivity of action, the cytotoxic effects of the developed systems were compared across both cancerous and normal cell lines. Furthermore, *in vitro* biocompatibility and targeted drug release studies were performed to validate the feasibility of these NPs for advanced biomedical applications.

Experimental

Materials and methods

All chemicals were used as received, without further purification. The following chemicals were purchased from Merck: ethylene glycol (EG, $C_2H_6O_2$), ethanol, sodium acetate (NaOAc, CH_3COONa), iron(III) chloride ($FeCl_3$), sodium citrate (Na_3Cit), tetraethyl orthosilicate (TEOS, $SiC_8H_2OO_4$), ethanolamine (EA, C_2H_7NO), cetyltrimethylammonium bromide (CTAB, $C_{19}H_{42}BrN$), NaOH, acetonitrile (C_2H_3N), calcium chloride ($CaCl_2$), (3-aminopropyl)triethoxysilane (APTES, $C_9H_{23}NO_3Si$), dimethyl sulfoxide (DMSO, C_2H_6OS), succinic anhydride ($C_4H_4O_3$), triethanolamine (TEAH3, $C_6H_{15}NO_3$), triethylamine (TEA, $(C_2H_5)_3N$), folic acid (FA, $C_6H_{15}NO_3$), EDC ($C_8H_{17}N_3$)/NHS ($C_4H_5NO_3$), capecitabine (CAPE, $C_{15}H_{22}FN_3O_6$), and curcumin (CUR, $C_{21}H_{20}O_6$). 2′,7′-Dichlorodihydrofluorescein diacetate (DCFH-DA), HME-1 (hTERT-HME1 [ME16C] (CRL-4010), ATTC) and MCF-7 cells (MCF7, (HTB-22) ATTC), and DMEM-F12 were purchased from Gibco.

Synthesis of superparamagnetic iron oxide nanoclusters (SPIONCs)

Superparamagnetic iron oxide nanoclusters (SPIONCs) were synthesized using a polyol method, as reported in detail earlier.[10] Briefly, $FeCl_3$ served as the iron source, while NaOAc acted as an alkali source, EG was used as a solvent and reducing agent, and Na_3Cit was used as the capping agent. Initially, a stock solution containing 200 mM $FeCl_3$ and 34 mM Na_3Cit was prepared in 100 mL of EG under continuous magnetic stirring until complete dissolution. Subsequently, 730 mM NaOAc was added to the solution, followed by additional stirring. The resulting mixture was transferred into a Teflon-lined stainless-steel autoclave (filling one-third of the total capacity), and the reaction was conducted at 220 °C for 15 h. The sample

Table 1 SPIONC sample designations (or generations) and functionality after various process steps

Code	Sample processing details	Sample designation/added functionality
G0	SPIONC	
G1	(Amorphous+) MPS-SPIONC	**G0** + MPS[a]
G1X	MPS-SPIONC-$CaCl_2$ (CTAB extraction)	**G1** − CTAB
G2	MPS-SPIONC-[$CaCl_2$]-NH_2	**G1X** + APTMS[b]
G3	MPS-SPIONC-[$CaCl_2$]-NH_2-COOH	**G2** + SA[c]
G4	MPS-SPIONC-[$CaCl_2$]-NH_2-COOH-FA	**G3** + FA[d]
G5	MPS-SPIONC-[$CaCl_2$]-NH_2-COOH-FA-CUR	**G4** + CUR[e]
G6	MPS-SPIONC-[$CaCl_2$]-NH_2-COOH-FA-CAPE	**G4** + CAPE[f]
G7	MPS-SPIONC-[$CaCl_2$]-NH_2-COOH-FA-CUR-CAPE	**G5** + CAPE or **G4** + CUR + CAPE

[a] Mesoporous silica. [b] (3-Aminopropyl)trimethoxysilane. [c] Succinic anhydride. [d] Folic acid. [e] Curcumin. [f] Capecitabine.

at this stage is designated as SPIONCs (**G0**), which is used for further coating and surface modification steps. Sample names are hereafter coded as G#, and the details are summarized in Table 1.

Synthesis of amorphous and mesoporous silica core–shell structures (MPS-SPIONCs)

To enhance steric stability and prevent aggregation, SPIONCs were coated with an amorphous silica layer *via* a sol–gel process. A stock solution of SPIONCs (13.1 mg of Fe_3O_4 in 0.26 mL of distilled water) was diluted in 7.74 mL of water and 30 mL of ethanol. Subsequently, 50 μL of TEOS was added, vortexed until a homogeneous solution was obtained, and sonicated for 2 min. Then, 0.2 mL of ethanolamine was introduced, followed by additional vortexing and incubation for 2 h. Following incubation, the solution was centrifuged at 8000 rpm for 15 min, and the precipitate was purified through sequential washing with deionized water and ethanol. The resulting amorphous silica-coated SPIONCs were magnetically separated and redispersed in 1 mL of Milli-Q water.[10,25] The silatrane complex was prepared by mixing and heating 11 mL of TEOS with 23 mL of TEAH3 until 140 °C for 5 min and then cooling down to room temperature. Thereafter, 6 mL of amorphous silica-coated SPIONCs, synthesized as described above, were dispersed in 6.24 mL of deionized water and sonicated. Separately, 0.12 g of CTAB was dissolved in 5.28 mL of ethanol, and the two solutions were combined and further sonicated. Thereafter, 936 μL of atrane was added, and the solution was incubated at room temperature for 24 h. Particles obtained after this step are designated as MPS-SPIONCs. The synthesized MPS-SPIONCs (**G1**) were purified by repeated washing with deionized water and ethanol.[25,26] The CTAB was extracted by a simple method; the sample was suspended in a mixture of EtOH : water (3 : 1 in volume) containing 500 mg of $CaCl_2$. The suspension was heated under reflux for 20 minutes. Finally, the particles were collected by centrifugation, washed with water and ethanol, and dried under vacuum at 40 °C. After the extraction process, the sample is given the code **G1X** (see Table 1).

Amine and carboxyl functionalization of MPS-SPIONCs

To introduce amine functional groups, 50 mg of MPS-SPIONCs (**G1X**) were dispersed in 2.5 mL of acetonitrile and sonicated for 15 min and then under continuous stirring. 50 μL of APTES was added, and the mixture was stirred at room temperature for 2 h. The resulting MPS-SPIONC-NH_2 (**G2**) was re-dispersed in 3 mL of DMSO, followed by the addition of 45 mg of succinic anhydride and 45 μL of TEA. The reaction proceeded at 50 °C for 48 h, yielding carboxyl-functionalized MPS-SPIONCs (MPS-SPIONC-NH_2-COOH).[27] The final product was purified *via* magnetic separation, ethanol washing, and vacuum drying. Particles obtained after this step are designated as MPS-SPIONC-NH_2-COOH (**G3**).

EDC/NHS activation and folic acid conjugation

To enable tumour-specific targeting, FA was conjugated onto MPS-SPIONC-NH_2-COOH (**G3**) *via* EDC/NHS coupling. 25 mg of EDC·HCl (0.161 mmol) and 12.5 mg of sulfur-NHS (0.108 mmol) were dissolved in DMSO and stirred for 2 h. In parallel, 20 mg of FA (0.044 mmol) was dissolved in 5 mL of anhydrous DMSO and then added to the EDC/NHS-activated solution. The reaction mixture was gently stirred at room temperature for 24 h, followed by washing with deionized water and vacuum drying.[28] Particles obtained after this step are designated as MPS-SPIONC-FA (**G4**).

Curcumin loading onto functionalized MPS-SPIONCs

CUR was loaded onto MPS-SPIONC-FA using a passive adsorption method. 50 mg of MPS-SPIONC-FA (**G4**) was dispersed in 12.5 mL of ethanol solution containing 4 mg mL^{-1} CUR and incubated at room temperature for 24 h in the dark. The CUR-loaded NPs were magnetically separated, and the supernatant was analysed using UV-Vis spectroscopy at 427 nm. CUR loading efficiency was calculated by subtracting the amount of CUR in the supernatant from the amount of CUR initially added, using the equation below:

$$\text{Drug loading efficiency } (\%) = \frac{\text{total amount of curcumin} - \text{free curcumin in the supernatant}}{\text{total amount of curcumin}} \times 100$$

A calibration curve was established using UV-Vis spectroscopy to determine CUR concentrations and loading efficiency, and the experiment was performed in six replicates.[27] Particles

obtained after this step are designated as MPS-SPIONC-FA-CUR (**G5**).

Capecitabine (CAPE) loading on functionalized MPS-SPIONCs

CAPE was loaded onto MPS-SPIONC-FA (**G4**) using the same procedure as mentioned above. 50 mg of MPS-SPIONC-FA was dispersed in 12.5 mL of ethanol solution containing 1 mg mL^{-1} CAPE and incubated at room temperature for 24 h. The CAPE-loaded NPs were magnetically separated, and the supernatant was analysed using UV-Vis spectroscopy at 307 nm. The drug-loading efficiency was calculated by using the equation below:[27]

$$\text{Drug loading efficiency (\%)} = \frac{\text{total amount of capecitabine} - \text{free capecitabine in the supernatant}}{\text{total amount of capecitabine}}$$

Particles obtained after this step are designated as MPS-SPIONC-FA-CAPE (**G6**).

A calibration curve was established using UV-Vis spectroscopy to determine CAPE concentrations and loading efficiency, and the experiment was performed in six replicates.[27]

Co-loading of CUR and CAPE onto MPS-SPIONCs

For dual drug loading, 50 mg of MPS-SPIONC-FA (**G4**) was first incubated in 12.5 mL of ethanol solution containing 4 mg mL^{-1} CUR under continuous shaking for 24 h. The CUR-loaded particles were separated and centrifuged at 8000 rpm for 5 min, followed by incubation with 12.5 mL of 1 mg mL^{-1} CAPE solution under the same conditions. The drug-loading efficiency for CUR and CAPE was calculated using previously established equations.[27] Particles obtained after this step are designated as MPS-SPIONC-FA-CUR-CAPE (**G7**).

Due to extensive processing and naming of the materials at various steps (or generations), we designated a code (G#) for each sample, starting with **G0** for SPIONCs. Table 1 summarizes sample designations after various process steps.

Drug release studies

The release kinetics of CUR and CAPE from drug-loaded MPS-SPIONC-FA were evaluated under different pH conditions (5.0, 6.5, and 7.4), simulating the tumour microenvironment and physiological conditions. The samples were incubated in phosphate-buffered saline (PBS) at 37 °C, and drug release was monitored using a microplate reader at 2-min intervals for 30 min. Absorbance values were measured at 427 nm for CUR and 307 nm for CAPE, after magnetic decantation, and cumulative release profiles were plotted.[27]

Characterization techniques

The hydrodynamic size and surface charge (ζ-potential) of the NPs were studied using dynamic light scattering (DLS) with a Zetasizer Nano ZS90 system (Malvern, UK) in aqueous suspension. The DLS measurements were reported as volume % values. The morphology and the internal structure of the NPs were analyzed using transmission electron microscopy (TEM; FEI TALOS F200S TEM 200 kV, Bayburt University-Türkiye). Samples for TEM were prepared by dropping 10 μL of NP suspension onto copper grids and allowing them to dry at room temperature. Additionally, scanning transmission electron microscopy (STEM) coupled with energy dispersive X-ray spectroscopy (EDS) was performed to determine the elemental distribution within the nanoclusters. Functional groups on NPs at various steps are evaluated by Fourier-transform infrared spectroscopy (FTIR; Thermo Fisher Scientific), using the ATR mode. UV-Vis measurements were performed using an Implen NanoPhotometer. The surface morphology and structural properties were further characterized using scanning electron microscopy (SEM). The specific surface area and porosity of the NPs were assessed *via* Brunauer–Emmett–Teller (BET) analysis. Nitrogen adsorption–desorption isotherms were recorded using an automated Micromeritics ASAP2020 instrument. Before the adsorption measurements, the samples were degassed in a vacuum (10^{-6} Torr) at 300 °C for 4 h to remove adsorbed gases. Magnetic properties were investigated at room temperature (T = 305 K) by vibrating sample magnetometry (VSM Quantum Design PMS9T), under a sweeping magnetic field from −20 kOe to +20 kOe. For magnetization measurements, 1 mL of NCs with a known concentration was taken in a centrifuge tube and dried, and thereafter 6 mg of the dried sample was placed directly into the vibrating sample magnetometer. The iron concentration was estimated by inductively coupled plasma optical emission spectroscopy (ICP-OES).

Cold atmospheric plasma (CAP)

The cold atmospheric plasma (CAP) source (Fig. S1) used in this study was developed by PACEM (Türkiye). The plasma system was designed to be compatible with He and Ar gases and operated in a temperature range of 25–40 °C, with a working frequency of 1 Hz to 10 kHz and a discharge power of 360 W. The system, powered by 32 V DC with a 100 kV AC output, generated alternating magnetic fields of 20 mW m^{-2} along the *xy*-axis and 12 mW m^{-2} along the *z*-axis. The plasma source operated at a radio frequency of ∼1 MHz with a voltage amplitude of 0–50 kV. The argon gas flow rate was fixed at 1 L min^{-1}, and the plasma was generated at the pin electrode tip, expanding outwards into the surrounding air. The distance between the plasma jet head and the surface of the 96-well plate was maintained at 15 mm (see the SI).

Cytotoxicity studies

This study utilized the human mammary epithelial cell line (HME-1) and the human breast adenocarcinoma cell line (MCF-7). The cells were maintained in Dulbecco's Modified Eagle Medium (DMEM, Gibco) supplemented with 10% fetal bovine serum (FBS) and 1% penicillin/streptomycin under standard

incubation conditions (5% CO_2, 37 °C).[29] The selectivity index (SI) serves as an indicator of NC types and CAP preferential cytotoxicity toward cancer cells over normal cells. A SI value above 3 indicates that the compound has high selectivity against cancer cells.[30,31] In this study, SI values were calculated by dividing the IC_{50} value obtained for the normal cell line (HME-1) by the IC_{50} value of the corresponding cancer cell line (MCF-7), as shown in the following equation:[32]

$$SI = \frac{IC_{50} \text{ for the normal cell line}}{IC_{50} \text{ for the cancer cell line}}$$

Cell viability assays

The cytotoxic effects of only CUR (0.5, 1, 1.5, 2, 2.5, 3, 3.5, 4, and 4.5 μg mL^{-1}) and only CAPE (0.005, 0.05, 0.1, 0.2, 0.4, 0.6, 0.8, 1, and 2 μg mL^{-1}) at various concentrations were investigated in MCF-7 cells for 24 h and 48 h.

Cytotoxicity of NCs

Cells were seeded into 96 well plates at 1×10^4 cells per well and incubated for 24 h in an environment containing 5% CO_2. Then, MNPs at various iron oxide nanoparticle concentrations (1, 2, 4, 6, 8, 10, 30, and 60 μg mL^{-1}) were added to the wells, and then the 96-well plates were placed on a MagnetoFactor-96 NdFeB magnetic plate (maximum surface magnetic field strength 0.3 Tesla; Chemicell, Germany) placed just below the culture plate to create a vertical magnetic field gradient. The plates were kept on this magnetic plate for 15 min in the incubator to maintain physiological temperature[33] and incubated for 24 h, 48 h, and 72 h. Following the treatment, the cells were washed with PBS twice to remove NCs, and then, 10% MTT solution was added to each well and incubated for 4 h. The medium was then replaced with 100 μL of DMSO, and the plates were kept in a dark environment for 30 min. Absorbance was measured at 560 nm using an Epoch microplate reader.

Cytotoxicity of CAP treatment

Each cell line was seeded in 96-well plates at a density of 1×10^4 cells per well. Once the cells reached confluency, the culture medium was removed and replaced with DMEM containing 1 M pyruvate. HME-1 and MCF-7 cells were treated with CAP for 5 s, 10 s, 15 s, 20 s, and 30 s and incubated for 24 h, 48 h, and 72 h. Following the treatment, 10% MTT solution was added to each well and incubated for 4 h. The medium was then replaced with 100 μL of DMSO, and the plates were kept in a dark environment for 30 min. Absorbance was measured at 560 nm using an Epoch microplate reader.

Cytotoxicity of the combination of CAP and NC treatment

Cells were seeded into 96 well plates at 1×10^4 cells per well and incubated for 24 h in an environment containing 5% CO_2. Then, MNPs at various NP concentrations (1, 2, 4, 6, 8, 10, 30, and 60 μg mL^{-1}) were added to the wells, and immediately the plates were placed on a MagnetoFactor-96 plate (Chemicell, Germany) for 15 min in an incubator.[33] Then, the cells were treated with CAP for 10 s and 20 s and incubated for 24 h and 48 h. Cell viability was monitored by the MTT protocol as described under the section ''Cytotoxicity of NCs''.

Reactive oxygen species (ROS) analysis

Intracellular ROS levels were determined using the DCFH-DA assay. Cells (1×10^4 per well) were incubated in complete culture medium for 24 h. Nanocluster (NC) suspensions (30 μg mL^{-1}) were added to the cells and incubated for 2 h. Each well was then treated with 100 μL of 25 μM DCFH-DA solution in PBS and incubated for 30 min. HME-1 and MCF-7 cells were exposed to CAP for 30 s. Fluorescence intensity was measured using a GloMax microplate reader (Promega, Germany) with an excitation wavelength of 460 nm and an emission wavelength of 500–550 nm.

Apoptosis assay

Apoptosis was evaluated using an Annexin V-FITC/PI Apoptosis Detection Kit (Elabscience). Cells exposed to CAP for 20 s and treated with 30 μg mL^{-1} **G4**, **G5**, **G6**, and **G7** nanoclusters were first washed twice with pre-cooled PBS at 4 °C, followed by centrifugation (2000*g*, 5 min). After removing the supernatant, 500 μL of binding buffer was added, and the cells were gently resuspended by pipetting. Subsequently, 5 μL of Annexin V-FITC and 5 μL of PI were added, mixed immediately, and incubated in the dark at room temperature for 5–15 min. Apoptosis was then measured using a NovoCyte3 130 flow cytometer with the FITC channel (excitation wavelength 480 nm) and the PE channel (excitation wavelength 540 nm), and the data were analyzed using NovoExpress 1.5.0 software.

Statistical analysis

Statistical analyses were performed using one-way/two-way analysis of variance (ANOVA), where appropriate (GraphPad Prism 8). Specifically, the *n* was 4 for cell culture studies and 3 for release studies. Data are presented as mean ± standard deviation (SD) unless otherwise specified. Statistical significance was denoted as follows: $p < 0.01$ (*), $p < 0.001$ (**), $p < 0.0001$ (***), $p < 0.00001$ (****), and $p < 0.000001$ (*****). Combination indices (CI) were calculated using CompuSyn software *via* the Chou–Talalay method. CI values <1, $=1$, and >1 indicated synergy, additivity, and antagonism, respectively.

Results and discussion

Classification and composition of NCs

NCs were categorized into eight distinct formulations based on surface modifications and cargo loading, as encoded in Table 1 and schematically shown in Fig. 1: unmodified superparamagnetic iron oxide nanocluster (SPIONC, **G0**), mesoporous silica-coated SPIONC (MPS-SPIONC, **G2**), folic acid-conjugated MPS-SPIONC (MPS-SPIONCFA, **G4**), CUR-loaded and FA-conjugated MPS-SPIONC (MPS-SPIONCFA-CUR, **G5**), capecitabine-loaded and FA-conjugated MPS-SPIONC (MPS-SPIONCFA-CAPE, **G6**),

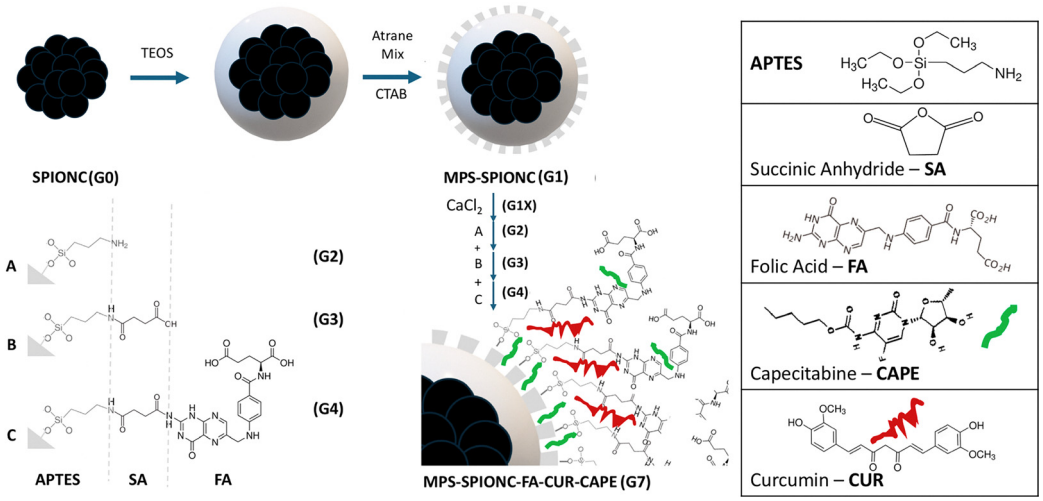

Fig. 1 A schematic presentation of nanocluster functionalization steps, including CTAB removal, surface modifications with APTES and succinic anhydride, EDC/NHS coupling, and sequential drug loading processes.

and dual drug-loaded (CUR-CAPE) and FA-conjugated MPS-SPIONC (MPS-SPIONCFA-CUR-CAPE, **G7**).

FT-IR analysis

Fourier-transform infrared (FTIR) spectroscopy was employed to verify surface modifications and conjugation steps for all nanoclusters at various process steps; the FT-IR spectra are presented in Fig. 2. Further spectra in segmented form are presented in Fig. S2. Table S1 lists the observed bands and their assignments, further confirming the success of conjugation at each step.

The characterization of the synthesized NCs demonstrated their structural and functional integrity following surface coating and drug loading. The FT-IR spectra of the SPIONCs (**G0**) showed absorption bands at 1633 and 1380 cm^{-1} (Fig. 2) associated with carboxylate, indicating the presence of carboxyl groups on their surface due to surface passivation with citrate ions. Similar carboxylate bands are consistent with previously reported FT-IR characterizations of citrate-coated iron oxide NPs.[34,35] Upon coating with amorphous and mesoporous silica layers (**G1**), signals due to the carboxyl (–COOH) groups of citrate diminished, while a new strong absorption band around 1070–1100 cm^{-1} appeared, indicative of Si–O–Si stretching. Similarly, the formation of strong Si–O–Si bands around 1080 cm^{-1} in the FT-IR spectra of silica-coated magnetic nanoparticles has been reported in the literature. These results confirm the successful silica encapsulation of sample **G1** obtained in our study.[34–36] Sample **G2** with APTMS modification of the surface showed the absence of OH vibrations, with new bands appearing around 3382 cm^{-1}, ascribed to the stretching vibrations of surface exposed N–H groups. Similar observations regarding FT-IR verification of amine functional groups were reported in previous studies on silica-coated SPIONs.[35,36] In the SA modified sample (**G3**), the absence of –OH vibrations suggests intramolecular interactions inhibiting free carboxyl groups. The reappearance of the –OH band in **G4** confirmed the presence of carboxyl groups from FA. These results agree well with the literature on the FT-IR characterization of folic acid-functionalized magnetic NPs.[36] However, in **G5** (MPS-SPIONC-$CaCl_2$-NH_2-COOH-FA-CUR), no –OH band corresponding to COOH was observed, suggesting that only SPIONC samples exhibited free carboxyl groups, likely due to intramolecular interactions. The FTIR spectrum of **G4** confirmed the conjugation of FA to MPS-SPIONC, with the presence of CAPE indicated by C═N stretching bands at 1610 cm^{-1} and 1613 cm^{-1} in both **G6** and **G7** samples.[37,38] Additionally, a weak band in the 1981–1967 cm^{-1} range suggested hydrogen bonding interactions. The FT-IR spectra of **G7** and **G6** exhibited dual peaks, likely due to modifications introducing characteristic hydrogen bonding interactions. This observation was additionally supported by the presence of characteristic vibrational peaks corresponding to COOH, NH/NH_2, C–N, C–H,

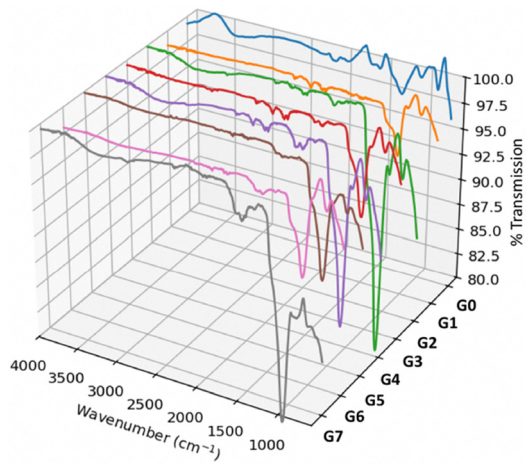

Fig. 2 FT-IR spectra of SPIONCs at various process steps, in the wavenumber range of 4000–600 cm^{-1}. Different NCs (G#) generated are displayed on the *y*-axis (**G0** – blue; **G1** – orange; **G2** – green; **G3** – red; **G4** – purple; **G5** – brown; **G6** – magenta; and **G7** – grey).

C–OH, and C=C bonds. However, the high silica content may have suppressed the bands for C–N, C–H, C–OH, and C=C, leading to a primary focus on COOH and NH/NH_2 vibrational modes.

According to Table S1, the $\delta(NH_2)$, $\nu_{as}(COO^-)$, $\nu_s(COO^-)$, and $\nu(C{=}O)$ bands were observed in the 1650–1400 cm^{-1} range, suggesting overlap between amino and carboxyl groups. The N–H bending vibration was observed between 1648 and 1632 cm^{-1}, potentially influenced by carbonyl groups. The carboxyl-related $\nu_{as}(COO^-)$ and $\nu_s(COO^-)$ bands were observed in the range of 1561–1555 cm^{-1}, appearing as shoulder peaks in **G5** (MPS-SPIONC-$CaCl_2$-NH_2-COOH-FA-CUR) and **G6** (MPS-SPIONC-$CaCl_2$-NH_2-COOH-FA-CAPE NCs), but more distinctly in **G7** (MPS-SPIONC-$CaCl_2$-NH_2-COOH-FA-CUR-CAPE). The co-loading of CUR and CAPE likely resulted in partial interactions that reduced individual FA–carboxyl interactions. The IR spectra of **G5** (MPS-SPIONC-$CaCl_2$-NH_2-COOH-FA-CUR) and **G7** (MPS-SPIONC-$CaCl_2$-NH_2-COOH-FA-CUR-CAPE) confirmed the presence of in-plane and out-of-plane bending vibrations (γ(CCH) + γ(CCC)) associated with CUR, particularly at 905 cm^{-1} (γ(CCH) + δ(CCH)).[14] These spectral shifts further supported the hypothesis that CUR and CAPE interact with FA, altering their interactions.

Surface charge

The zeta potential of SPIONCs after surface modifications was evaluated, and it was shown that each functionalization step provides systematic control over the surface charge. Zeta potential measurements, presented in Fig. 3, showed alternating positive and negative surface charges in the surface functionalization stage. The as-made SPIONCs (**G0**) bear a negative charge (−19 mV) due to capping with citrate molecules. Upon coating with mesoporous silica-MPS (**G1**), the zeta potential becomes more negative (−26.1 mV) due to the silanol groups on the surface of silica, which impart a more anionic characteristic to the surface and increase electrostatic stability. Amine functionalization reverses the surface charge to positive, due to the protonation of the amines (**G2**). Surface modification with amine (NH_2) groups significantly increased the zeta potential, yielding a value of +29.1 mV for the MPS-SPIONC-$CaCl_2$-NH_2 sample. This indicates that the surface acquired the anticipated positive character, confirming successful amine modification. However, after functionalization with carboxyl (COOH) groups through EDC/NHS coupling (**G3**), the zeta potential dropped to −28.7 mV, confirming that the modification was successful and precisely controlled.[39] FA conjugation slightly reduces the magnitude of charge, due to FA possessing both amine and carboxyl groups, while still maintaining the overall negative charge (**G4**). Since FA contains both COOH and NH_3^+ terminal groups, a specific binding strategy was applied. Through EDC/NHS activation, the NH_3^+ group of FA was directed to bind to the negatively charged **G3** surface, allowing the COOH end to remain free for potential interaction with folate receptors (FRs) on target cancer cells.[10,27] Following FA conjugation, a zeta potential of −8.18 mV was measured for the MPS-SPIONC-FA (**G4**). This approach slightly reduced the negative surface charge, and FA was successfully conjugated while maintaining its targeting ability. After CUR loading, the zeta potential of **G5** (MPS-SPIONC-FA-CUR) was measured to be +25.2 mV and that of CAPE-loaded NC **G6** was measured to be −7.23 mV. CUR is a hydrophobic molecule, which is expected to intercalate between the hydrophobic chains of surface modifying coupling entities, thus reducing the contribution of surface silanol groups to the measured overall charge density of FA coated SPIONCs (**G5**). The average zeta potential of CUR is −5.94 mV,[40] and CUR introduction to the SPIONCs can decrease the apparent zeta potential to more negative values, but CUR can also bring out a reverse effect on the charge.[41] Based on the literature, co-introducing CUR and FA can show a neutral, increasing, or decreasing effect on the NPs' zeta potential.[42–44] It is known that CUR undergoes keto–enol tautomerism and this defines its pK_a values as ∼8.4 (pK_{a1}), 9.9 (pK_{a2}), and 10.5 (pK_{a3});[45] pH > 7 deprotonation starts for CUR.[46] The zeta potentials were tested in DI water, at pH < 7.0, so the protonated form of CUR may dominate the observed positive charge (**G5**). Therefore, we can claim that the surface chemistry of NPs is a factor determining how CUR alters the zeta potential of the formulation. CAPE is an amphiphilic molecule, which can even fill the pores of mesoporous silica if part of the pores are accessible, not significantly influencing the measured surface charge density of FA coated SPIONCs (**G7**).

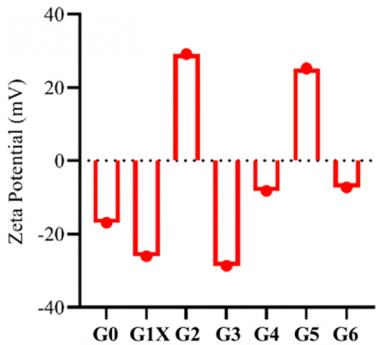

Fig. 3 Zeta potential values of the SPIONCs after various process steps. For sample designations, see Table 1.

Size and morphology – DLS and TEM analyses

Dynamic light scattering (DLS) analysis was used to study the hydrodynamic size of the SPIONCs after some processing steps. DLS results for the SPIONC (**G0**), mesoporous silica coated MPS-SPION (**G2**), and, after folic acid conjugation, MPS-SPIONC-FA (**G4**) are presented in Fig. 4. Average hydrodynamic sizes are estimated to be 167 ± 38 nm for SPIONC (**G0**), 318 ± 77 nm for MPS-SPIONC (**G2**), and 350 ± 52 nm for MPS-SPIONCFA (**G4**). The increase of the average size going from SPIONCs (**G0**) to MPS-SPIONCs (**G2**) suggests a silica (amorphous and mesoporous silica) coating thickness of about 75 nm. Finally, upon NHS/EDC coupling followed by FA conjugation, the average radius is further increased by about 15 nm, which also includes the solvation layer on the MPS-SPIONC-FA (**G4**).

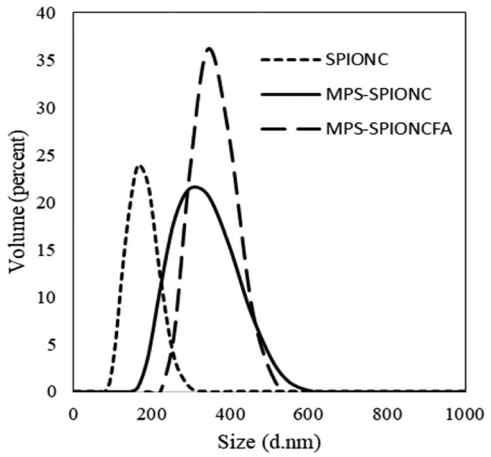

Fig. 4 Dynamic light scattering (DLS) analysis of SPIONCs showing the particle size distribution profile based on volume percent for the SPIONC (**G0**), MPS-SPIONC (**G2**), and MPS-SPIONC-FA (**G4**).

TEM micrographs and elemental mapping of SPIONC at various processing steps are presented in Fig. 5 and 6. The micrographs show the evolution of SPIONCs (Fig. 5(a)) with amorphous silica coating (Fig. 5(b)) followed by the mesoporous silica coating (Fig. 5(c)). From the micrographs, the thickness of the amorphous layer is estimated to be 25 nm, while that of the mesoporous layer is approximately 50 nm, resulting in an overall increase of SPIONCs by about 75 nm, in agreement with the estimation from the DLS data. MPS-SPIONCs are intact upon loading of CUR, as shown in Fig. 5(d) (MPS-SPIONCFA-CUR). However, degradation of the silica layer is observed when the MPS-SPIONCs are loaded with CAPE alone (Fig. 5(e)) or CUR loading followed by CAPE, as shown in Fig. 5(f) (MPS-SPIONCFA-CUR-CAPE).

STEM mapping of NCs is also performed at various process steps and is presented in Fig. 6 for MPS-SPIONC (Fig. 6(a)), MPS-SPIONC-FA-CUR (Fig. 6(b)), and MPS-SPIONCFA-CAPE (Fig. 6(c)). Elemental mapping clearly indicates the presence of iron oxide in the core of the MPS-SPIONC, while the Si signal arises from the conformally coated SiO_2 layer surrounding the core (Fig. 6(a)). MPS-SPIONCFA-CUR shows additional Ca and Cl signals, which are due to the extraction of CTAB from the mesoporous silica system using $CaCl_2$ (Fig. S6b). As CUR is composed of C, O, and H, there is no specific elemental signal to confirm its presence. In the mapping of the MPS-SPIONCFA-CAPE sample (Fig. 6(b)), there are additional signals of N and F derived from CAPE, confirming its presence on the SPIONCs.

Porosity and surface area – BET analysis

In this study, CTAB is used as a pore template agent during the formation of the mesoporous silica structure; however, it must be removed after synthesis as it blocks the pores and negatively affects biocompatibility. Moreover, the pores must be open and accessible for applications such as drug loading.[25] Therefore, CTAB was removed using a simple ion-exchange method, using $CaCl_2$ instead of NaCl, as reported in earlier reports.[25] This approach effectively removed the surfactant from the structure. Nitrogen adsorption–desorption isotherms were obtained to evaluate the surface area and porosity of MPS-SPIONCs, as presented in Fig. S3. The porous nature of the material is evident in the nitrogen adsorption–desorption isotherms and the pore distribution (Fig. S4). The isotherm (Fig. S4(a))

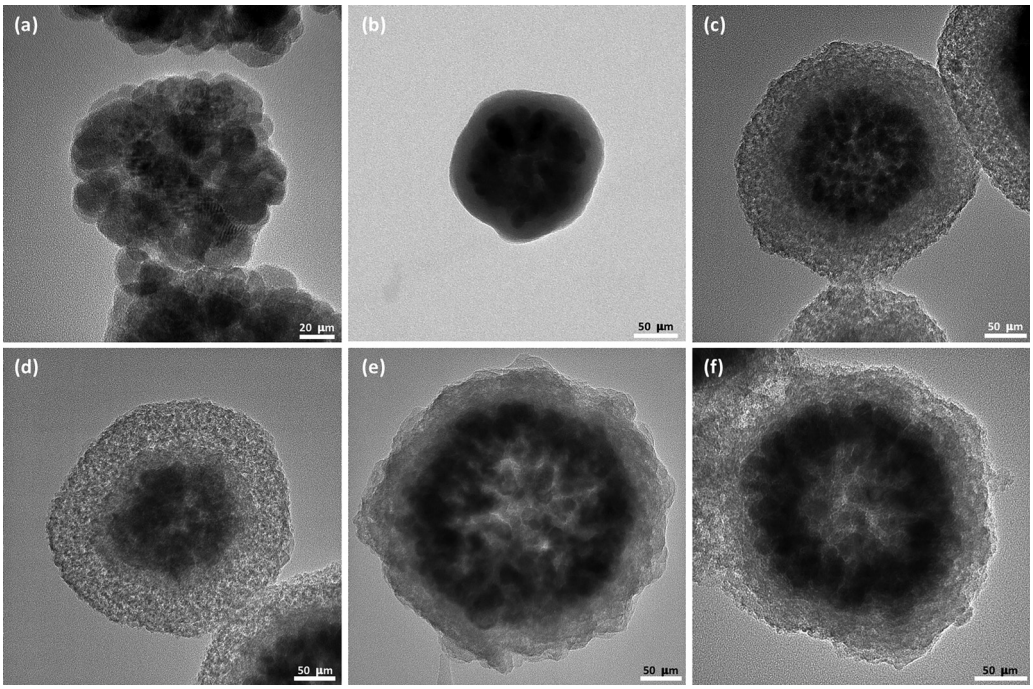

Fig. 5 TEM micrographs of (a) SPIONC-**G0**, (b) amorphous silica coated SPIONCs, (c) MPS-SPIONCs after extraction of CTAB-**G1X**, (d) MPS-SPIONCFA-CUR-**G5**, (e) MPS-SPIONCFA-CAPE-**G6**, and (f) MPS-SPIONCFA-CUR-CAPE-**G7**.

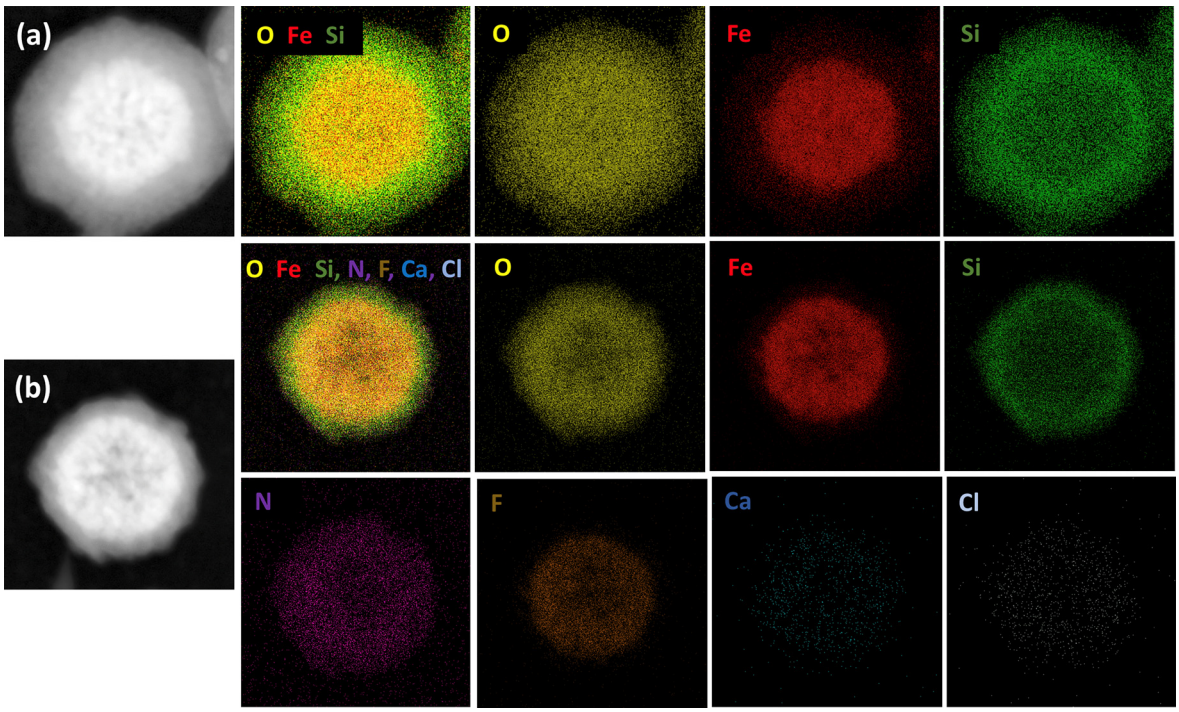

Fig. 6 STEM mapping images of NCs: (a) MPS-SPIONC – **G2** and (b) MPS-SPIONCFA-CAPE – **G6**.

displayed a well-defined adsorption step between the relative pressure of 0.1 and 0.4, corresponding to the condensation of the nitrogen inside the mesopores obtained using the CTAB as a template. It is important to note that the thickness of the mesoporous silica layer is around 50 nm and the core contains heavy elements. Knowing this, the surface area and the pore volume (surface 417 $m^2\ g^{-1}$ and volume 0.23 $cm^3\ g^{-1}$) are significant. The pore size distribution (Fig. S4b) shows a maximum centered at 2.5 nm which corresponds to the surfactant micelles. This strategy has completely removed the CTAB from the pores, as demonstrated in our earlier work.

Magnetic properties – VSM analysis

Vibrating sample magnetometry (VSM) was employed to assess magnetic behaviour before and after surface modifications. The results are presented in Fig. 7(a) for **G0**, normalized to the weight of Fe_3O_4. In Fig. 7(b), the magnetization results for **G2**, **G4**, **G5**, and **G6** are presented in comparison to uncoated **G0**, each normalized to the overall sample weight after sequential coating with amorphous and mesoporous silica, the functionalization, and the drug loading. The uncoated SPIONC, **G0**, showed a saturation magnetization at around 79 emu g^{-1} Fe_3O_4 (normalized to the weight of Fe_3O_4), indicating its strong superparamagnetic characteristics. Recent studies have demonstrated that synthesizing SPIONs in clustered architectures can enhance magnetization per secondary particle – SPIONCs.[25] After the coating steps, surface modification and functionalization, and drug loading, a significant decrease in saturation magnetization normalized to the overall sample weight was observed due to the addition of nonmagnetic layers

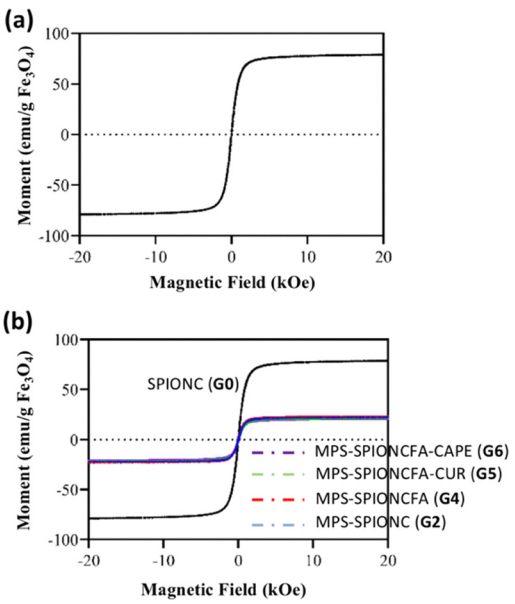

Fig. 7 Magnetization curves of (a) **G0** normalized to the weight of Fe_3O_4 and (b) **G0** compared with **G2**, **G4**, **G5**, and **G6**, each normalized to the overall sample weight after sequential coating with amorphous silica and mesoporous silica.

(amorphous and mesoporous silica) and organic molecules. Furthermore, the retention of saturation magnetization at around 21 emu g^{-1} and the maintenance of superparamagnetic characteristics following silica-based coatings indicate that the magnetic core remains stable and functional. These findings

suggest that while the magnetic response is reduced, NCs remain sufficiently responsive for interaction with the external magnetic field.

Drug loading capacity – UV-Vis spectroscopy

CUR and CAPE loading efficiencies were quantified using UV-Vis spectroscopy at respective wavelengths: CUR at λ = 427 nm and CAPE at λ = 307 nm. A calibration curve was constructed, revealing average loading capacities of ~25% for CUR and ~8% for CAPE when loaded independently. However, when CUR and CAPE were loaded together into NCs, the loading capacities were 14% for CUR and 4% for CAPE. These data confirm that the MPS-functionalized FA-conjugated SPIONCs effectively encapsulate both hydrophobic and hydrophilic drugs.

Release profiles of CUR and/or CAPE from NCs

The cumulative *in vitro* release profiles of CUR and CAPE from functionalized SPIONCs were assessed under physiologically relevant conditions at pH 5.0 (lysosomal), 6.5 (tumor microenvironment), and 7.4 (physiological blood pH). The drug-loaded NCs were incubated in phosphate-buffered saline (PBS) adjusted to the respective pH values. Samples were collected every 5 min over a 60 min period, and the release was monitored using UV-Vis spectroscopy (Fig. 8(a)–(d)). At pH 5.0, a significantly higher release rate was recorded for both CUR and CAPE, consistent with the protonation of surface groups under acidic conditions. At pH 6.5, intermediate release was observed, aligning with the mildly acidic tumour extracellular environment. At pH 7.4, minimal release was observed, indicating the structural stability of the nanocarriers under physiological conditions and their potential for stimuli-responsive, targeted release in acidic tumour compartments. Specifically, for only CUR-loaded NCs, the maximum drug release was observed at pH 5.0, whereas for only CAPE-loaded NCs, the highest release occurred at both pH 5.0 and pH 6.5. In dual CUR and CAPE loaded SPIONCs, CUR exhibited maximum release at pH 6.5, while CAPE showed its highest release at pH 5.0.

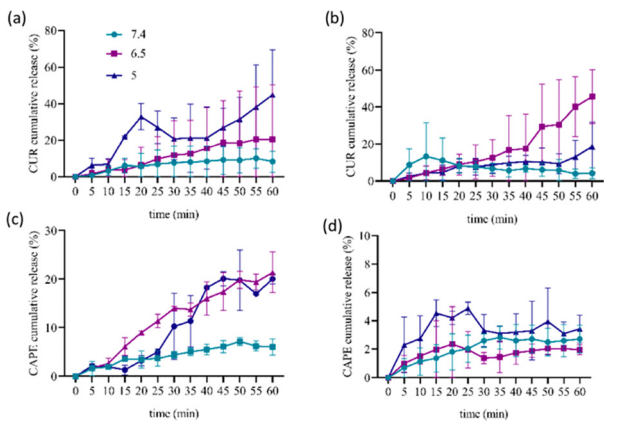

Fig. 8 CUR and CAPE release from NCs at pH 5, 6.5, and 7.4. (a) CUR release from **G5**, (b) CUR release from **G7**, (c) CAPE release from **G6**, and (d) CAPE release from **G7**.

The inclusion of CAPE and CUR in the formulation together may lead to increased drug–drug or drug–organic groups interactions, thus limiting the mobility of CAPE. The lipophilic structure of CUR may have caused CAPE to be confined to the inner regions of the nanostructure and prevented its diffusion to the external environment. CUR has two hydrophobic phenyl domains which can participate in π–π van der Waals interactions with aromatic amino acid side chains. CUR binds to DNA by hydrogen bonding interactions with the minor groove in AT-rich regions.[47] CAPE binds to ctDNA and hydrogen bond was the main force during binding.[48] This may suggest that physical interactions, such as hydrogen bonds or π–π interactions, may take place between the two compounds. The interaction of CAPE and CUR may have led to low release, as shown in Fig. 8(d). These findings confirm that the MPS-SPIONC-FA platform supports pH-sensitive drug release, enhancing controlled release within tumor environments while minimizing premature release in the systemic circulation.

Cytotoxic effects

Cytotoxic effect of cold atmospheric plasma (CAP) on HME-1 cells. The assays were performed *in vitro* under atmospheric argon plasma conditions, and the cytotoxicity was measured at 24 h. 30 s CAP treatment led to a 44% decrease in cell viability. These findings demonstrate that CAP exerts a dose- and time-dependent cytotoxic effect on HME1 cells, as shown in Fig. 9(a)–(c), which are relatively resistant to CAP because IC_{50} values are always above 30 s with CAP treatment.

Cytotoxic effect of cold atmospheric plasma (CAP) on MCF-7 cells. CAP treatment applied to the MCF-7 cell line for 24 h, 48 h, and 72 h resulted in statistically significant and time-dependent reductions in cell viability compared to the control group for each incubation time, as presented in Fig. 9. Across all incubation times, treatments ranging from 5 s to 30 s led to significant

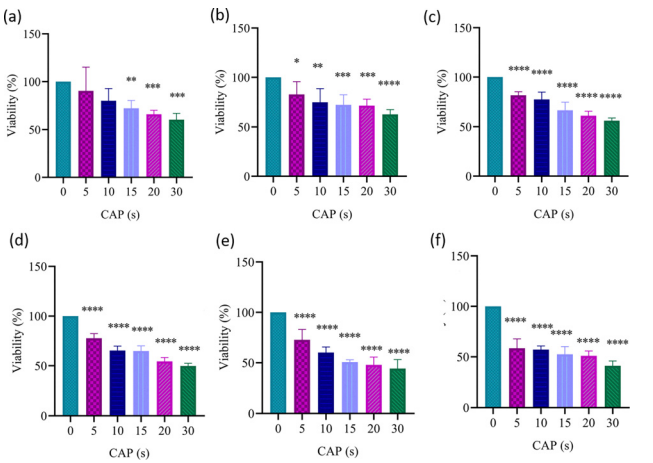

Fig. 9 Effect of CAP on the cytotoxicity of MCF-7 cells at different exposure times and incubation periods. Cells were treated with CAP for 0, 5, 10, 15, 20, or 30 s and incubated for (a) HME1 cell viability for 24 h, (b) HME1 cell viability for 48 h, and (c) HME1 cell viability for 72 h, (d) MCF-7 cell viability for 24 h, (e) MCF7 cell viability ($p < 0.01$ (*), $p < 0.001$ (**), $p < 0.0001$ (***), $p < 0.00001$ (****)).

differences compared to the control group ($P < 0.0001$). The most pronounced effect was observed at 30 s, with the cell viability decreasing to approximately 50% at 24 h and 41% at 72 h.

The IC_{50} values observed in MCF-7 cells were 29 ± 2 s at 24 h in Fig. 9(d), 17 ± 3 s at 48 h in Fig. 9(e), and 21 ± 5 s at 72 h in Fig. 9(f). The IC_{50} values are shown in Table S2. These results indicate that CAP exerts a strong and progressively increasing cytotoxic effect on MCF-7 cells, with the highest sensitivity observed at 48 h.

According to our findings, while the IC_{50} value decreased significantly over time in MCF-7 cells after CAP application, this value was relatively high in HME-1 cells. Despite increased CAP exposure, the IC_{50} value could not be reached in HME-1 cells even at 24 h, 48 h, or 72 h. This result clearly showed that the cytotoxic effect of CAP was higher against cancer cells than normal cells. Similarly, it has been reported that CAP may have cell-type-specific effects.[49,50] The cytotoxicity of CAP against cancer cells was proposed to be through apoptosis and ROS.[20,21,51] The rapid decrease in IC_{50} observed between 24 h and 48 h in MCF-7 cells following CAP treatment has been associated with mechanisms such as mitochondrial destruction, cell membrane damage, and DNA fragmentation.[21] While most CAP applications have traditionally focused on skin wound healing, studies investigating its effects in oncology have primarily used *in vitro* and *in vivo* models. Clinical observations also support the potential of CAP in cancer treatment. For example, Metelmann *et al.*[52] reported significant benefits in cancer patients, including reduced pain medication requirements, reduced microbial burden-related odour, and weight gain. Furthermore, other studies have suggested that CAP palliation may improve quality of life and even prolong survival in patients with advanced oropharyngeal cancer.[53,54] Current evidence suggests that CAP therapy increases cytotoxicity in cancer cells over time while exhibiting relatively less severe effects on healthy cells, thus offering a window of therapeutic selectivity. While studies on the application of CAP in cancer are limited, ongoing research continues to explore its potential. Collectively, these findings provide a strong rationale for considering CAP as a complementary oncological treatment.

Cytotoxicity of SPIONCs in HME-1 cells

In HME-1 cells, unmodified SPIONCs exhibited limited cytotoxicity, with significant reductions in cell viability observed only at the highest concentrations of 30 and 60 μg mL^{-1} ($P < 0.001$) at 24 h. However, MPS-functionalized formulations exhibited enhanced cytotoxic effects even at lower concentrations at 24 h. MPS-SPIONCs induced a significant reduction in cell viability starting from 2 μg mL^{-1} ($P = 0.0114$), while MPS-SPIONC-FA exhibited cytotoxic effects beginning at 1 μg mL^{-1} ($P = 0.0018$). Moreover, **G5**, **G6**, and **G7** formulations all triggered early and exhibited cytotoxicity from 1 μg mL^{-1} ($P < 0.0001$). Notably, at 60 μg mL^{-1}, cell viability in the dual-drug-loaded group **G7** decreased dramatically to 40% (Fig. 10(a)).

At 48 h, **G2** exhibited mild yet statistically significant cytotoxicity across all concentrations, with the cell viability decreasing to 73.45% at 60 μg mL^{-1} (Fig. 10(b)). In contrast, MPS-coated and drug-loaded NCs demonstrated stronger, dose-dependent cytotoxic effects. Specifically, **G6** reduced cell viability to 12%, **G5** to 21%, and **G7** to 27% at 60 μg mL^{-1}. IC_{50} values corroborated these findings, indicating moderate to high cytotoxicity, particularly in the drug-loaded groups.

Moderate cytotoxicity was observed for **G2** (IC_{50} = 32 ± 3 μg mL^{-1}), **G4** (IC_{50} = 33 ± 3 μg mL^{-1}), and **G5** (IC_{50} = 29 ± 2 μg mL^{-1}), **G6** (19.87 ± 2.13 μg mL^{-1}), and **G7** (24.38 ± 3.88 μg mL^{-1}).

At 72 h, cytotoxic effects were further enhanced, with the majority of NCs reaching their IC_{50} thresholds (Fig. 10(c)). The IC_{50} values at this time point were 26 ± 4 μg mL^{-1} for **G7**, 21 ± 2 μg mL^{-1} for **G6**, 32 ± 4 μg mL^{-1} for **G5**, and 48 ± 4 μg mL^{-1} for **G2**. The IC_{50} values are summarized in Table S3.

Cytotoxicity of NCs in MCF-7 cells

The cytotoxic effects of SPIONC-based NPs, functionalized with various targeting and therapeutic biomolecules, were evaluated in MCF-7 breast cancer cells over 24 h, 48 h, and 72 h (Fig. 11). At 24 h, there were no significant differences between any of the groups and the control ($P > 0.9999$). However, starting from 1 to 2 μg mL^{-1}, clear differences appeared: **G7** exhibited much stronger cytotoxicity than SPIONC ($P < 0.0001$). Between 4 and 10 μg mL^{-1}, the CAPE-loaded and dual drug-loaded formulations caused a significant decrease in cell viability ($P < 0.001$–0.0001). The strongest cytotoxic effects were seen at 30 and 60 μg mL^{-1}, especially in the CUR- and/or CAPE-containing NCs ($P < 0.0001$, Fig. 11(a)). At this time point, the lowest IC_{50} values were found in the **G7** (26 ± 6 μg mL^{-1}), **G6** (34 ± 3 μg mL^{-1}), and **G5** (47 ± 10 μg mL^{-1}) groups.

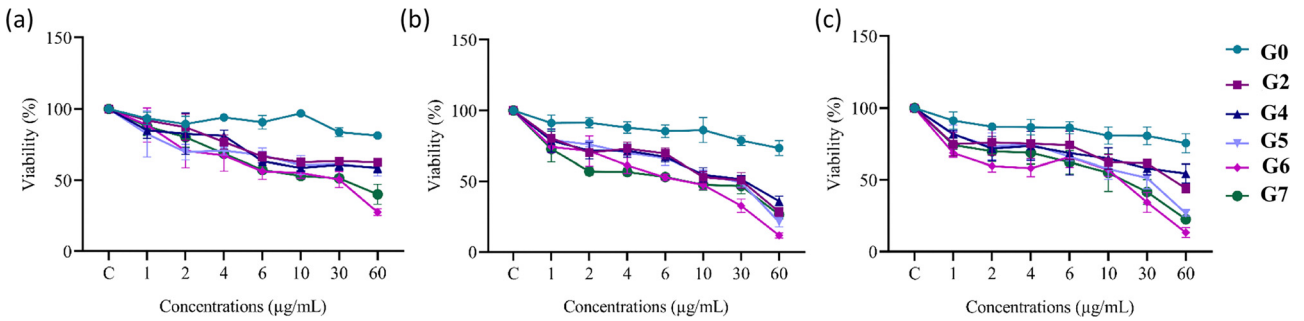

Fig. 10 Concentration-dependent effects of different SPION-based nanoparticle groups on cell viability in HME1 cells at (a) 24 h, (b) 48 h, and (c) 72 h post-incubation. (C designates control cells with no NPs.)

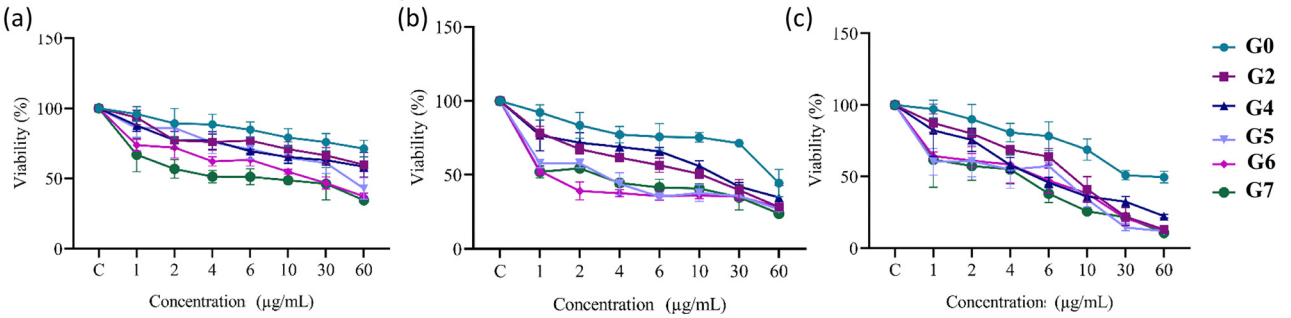

Fig. 11 Concentration-dependent effects of different SPION-based nanoparticle groups on cell viability in MCF-7 cells at (a) 24 h, (b) 48 h, and (c) 72 h post-incubation. (C designates control cells with no NPs.)

By 48 h, all NP-treated groups showed statistically significant reductions in cell viability compared to the control. SPIONCs exhibited mild cytotoxicity starting at 2 μg mL^{-1}, while functionalized NCs containing FA, CUR, or CAPE exhibited significant cytotoxic effects from as low as 1 μg mL^{-1} ($P <$ 0.0001). The lowest viability at 60 μg mL^{-1} was observed in the **G7**, **G6**, and **G5** groups (Fig. 11(b)). IC_{50} values at 48 h for these NCs were calculated to be 13 ± 2, 5 ± 4, and 13 ± 2 μg mL^{-1}, respectively. At 72 h, even SPIONCs alone caused significant cytotoxicity, starting from 4 μg mL^{-1} and above ($P < 0.01$). All functionalized nanoparticles exhibited strong and significant cytotoxic effects starting from 1 to 2 μg mL^{-1} ($P < 0.0001$). The biggest drop in cell viability at 60 μg mL^{-1} was seen in the **G7** (IC_{50} 10 ± 6 μg mL^{-1}), **G6** (IC_{50} 14 ± 3 μg mL^{-1}), and **G5** (IC_{50} 13 ± 1 μg mL^{-1}) groups (Fig. 11(c)). These findings indicate that cytotoxicity increases with longer exposure, especially in drug-loaded NCs. The IC_{50} values are shown in Table S4.

The cytotoxicities of CUR at concentrations of 0, 0.5, 1, 1.5, 2, 2.5, 3, 3.5, 4, and 4.5 μg mL^{-1} and CAPE at concentrations of 5 ng mL^{-1}, 50 ng mL^{-1}, 0.1, 0.2, 0.4, 0.6, 0.8, 1, and 2 μg mL^{-1} alone were also assessed as positive controls for incubation periods of 24 h and 48 h in MCF-7 cells (Fig. S5). However, since cell viability did not decrease below 50% for CUR and CAPE, IC_{50} values could not be determined at 24 h and 48 h (Fig. S5a and b).

In CUR-loaded NCs, 2.4 μg mL^{-1} CUR was present at a dose of 30 μg mL^{-1} NCs. While the IC_{50} value of CUR-loaded NCs was 47 ± 10 μg mL^{-1}, the IC_{50} value was not reached even at the highest dose (4.5 μg mL^{-1}) in MCF-7 cells treated with only CUR. In CAPE-loaded NCs, 0.24 μg mL^{-1} CAPE was present at a dose of 30 μg mL^{-1} NCs. While the IC_{50} value of CAPE-loaded NCs was 34 ± 3 μg mL^{-1}, the IC_{50} value was not reached even at the highest dose (2 μg mL^{-1}) in MCF-7 cells treated with only CAPE. When the cytotoxicity of CUR- and CAPE-loaded NCs was compared with that of free CUR and CAPE, the drug-loaded NCs were found to be more effective even at very low doses.

Cytotoxic effects of combined NC and CAP applications on HME-1 cells

Following SPIONC treatment, the cells were exposed to CAP for 0 s, 10 s, or 20 s, and viability was assessed at 24 h and 48 h. The results are presented in Fig. 12 and 13. At 24 h, following 20 s CAP exposure, the NCs with IC_{50} values below 30 μg mL^{-1} were **G5** (28 ± 16 μg mL^{-1}) and **G6** (16 ± 5 μg mL^{-1}). The IC_{50} values are shown in Table S5. These values illustrate a clear CAP-duration-dependent enhancement of NC cytotoxicity (p-values consistently below 0.0001 under prolonged CAP exposure).

At 48 h, the application of NCs and CAP together in HME1 cells showed a more cytotoxic effect compared to that at 24 h in all groups (Fig. 13). At the end of 10 s and 20 s CAP application in all groups, cytotoxicity increased significantly ($p < 0.05$ to $p < 0.001$). It is seen that the toxicity developed due to CAP application in **G4** is more than that in **G2**. This shows that FA increased the toxic effect in HME1 cells at 48 h. CUR loading in

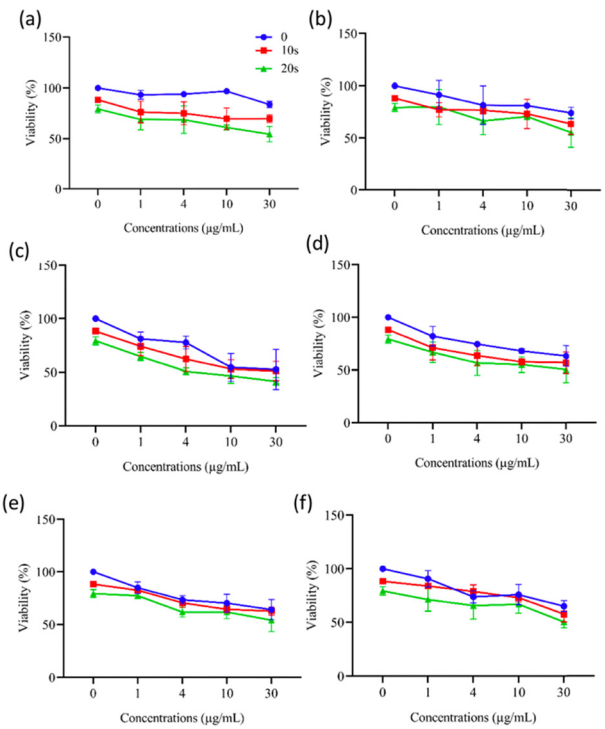

Fig. 12 Evaluation of the cytotoxicity resulting from the 24 h co-treatment of HME-1 cells with NCs and CAP using the MTT assay: (a) **G0**, (b) **G2**, (c) **G4**, (d) **G5**, (e) **G6**, and (f) **G7**. For sample designations, see Table 1. Statistical analysis was performed using a two-way ANOVA with multiple comparisons, where the 0 s CAP application (blue, top) was compared with the 10 s (red, middle) and 20 s (green, bottom) applications.

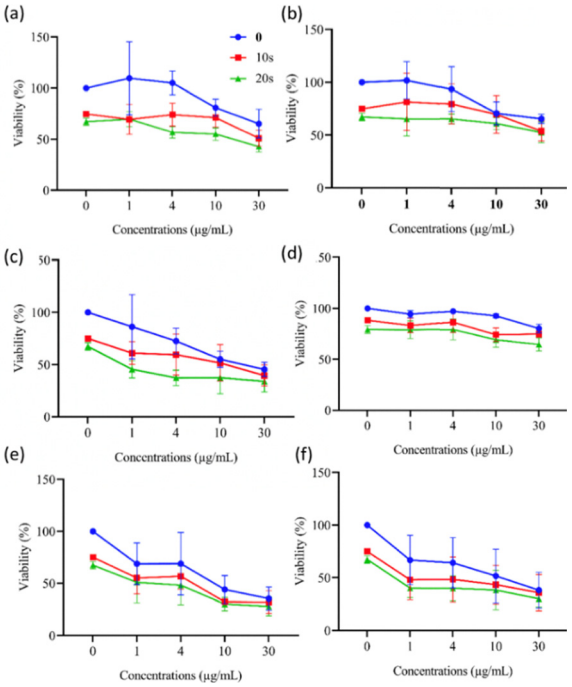

Fig. 13 Evaluation of the cytotoxicity resulting from the 48 h co-treatment of HME-1 cells with NCs and CAP using the MTT assay: (a) **G0**, (b) **G2**, (c) **G4**, (d) **G5**, (e) **G6**, and (f) **G7**. For sample designations, see Table 1. Statistical analysis was performed using a two-way ANOVA with multiple comparisons, where the 0 s CAP application (blue, top) was compared with the 10 s (red, middle) and 20 s (green, bottom) applications.

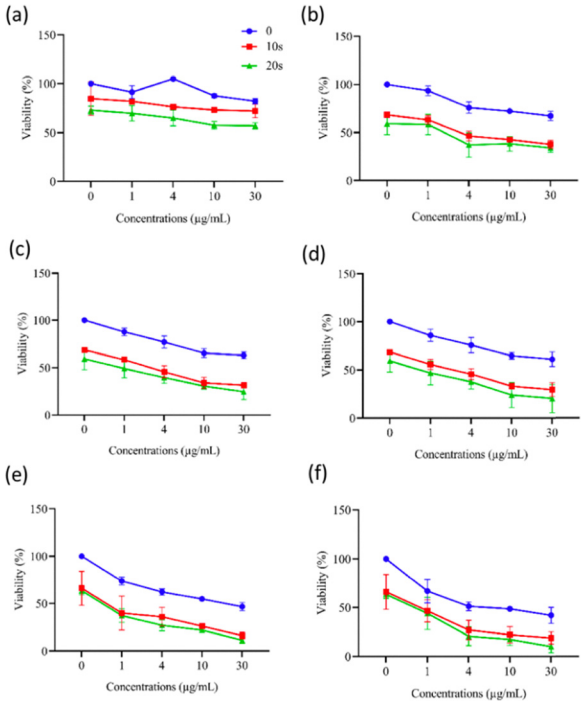

Fig. 14 Evaluation of the cytotoxicity resulting from the 24 h co-treatment of MCF-7 cells with NCs and CAP using the MTT assay: (a) **G0**, (b) **G2**, (c) **G4**, (d) **G5**, (e) **G6**, and (f) **G7**. For sample designations, see Table 1. Statistical analysis was performed using a two-way ANOVA with multiple comparisons, where the 0 s CAP application (blue, top) was compared with the 10 s (red, middle) and 20 s (green, bottom) applications.

G4 decreased the toxicity compared to those functionalized with FA only. After CAP application, the IC_{50} values of FA-loaded NCs (**G4**) decreased dramatically (19 ± 6 μg mL^{-1} (0 s), 10 ± 6 μg mL^{-1} (10 s), 0.5 ± 0.1 μg mL^{-1} (20 s)), while the decrease in IC_{50} values of CUR-loaded ones (**G5**) remained small (28 ± 16 μg mL^{-1} (20 s)). The IC_{50} values of CAPE-loaded NCs (**G6**) were 8.7 ± 6.1 μg mL^{-1} (0 s), 2.84 ± 1.32 μg mL^{-1} (10 s), and 1.5 ± 0.5 μg mL^{-1} (20 s). The IC_{50} values of CUR and CAPE-loaded NCs were calculated to be 11 ± 6 μg mL^{-1} (0 s), 1.09 ± 0.03 μg mL^{-1} (10 s), and 0.06 ± 0.08 μg mL^{-1} (20 s). After CAP exposure, the IC_{50} values of CUR-loaded NCs (**G5**) are generally greater than 30 μg mL^{-1}. The IC_{50} values are summarized in Table S6.

Cytotoxic effects of combined NC and CAP applications on MCF-7 cells

Following SPIONC treatment, the cells were exposed to CAP for 0 s, 10 s, or 20 s, and viability was assessed at 24 h and 48 h. At 24 h, significant differences in cytotoxicity occurred between mesoporous-silica coated NCs treated with CAP and those not treated with CAP in MCF-7 cells (Fig. 14). IC_{50} values after 10 s and 20 s CAP application were calculated as follows: 4.25 ± 1.28 to 1.82 ± 0.42 μg mL^{-1} for **G2**, 2.38 ± 0.36 to 0.89 ± 0.01 μg mL^{-1} for **G4**, 1.96 ± 0.19 to 0.69 ± 0.04 μg mL^{-1} for **G5**, 0.33 ± 0.07 to 0.19 ± 0.02 μg mL^{-1} for **G6**, and 0.43 ± 0.09 to 0.36 ± 0.08 μg mL^{-1} for **G7**. The IC_{50} values are presented in Table S7. IC_{50} values at 48 h were calculated as follows (Fig. 15): 4.24 ± 0.33 to 0.61 ± 0.07 μg mL^{-1} for **G0**, 15.16 ± 1.97 to 0.01 ± 0.02 μg mL^{-1} for **G2**, 2.95 ± 0.80 to 0.39 ± 0.04 μg mL^{-1} for **G4**, 1.47 ± 0.13 to 0.35 ± 0.05 μg mL^{-1} for **G5**, 2.80 ± 0.64 to 0.89 ± 0.02 μg mL^{-1} for **G6**, and 0.80 ± 0.05 to 0.13 ± 0.06 μg mL^{-1} for **G7**. The IC_{50} values are summarized in Table S8.

After CAP exposure, the SI values of CUR-CAPE loaded NCs (**G7**) were less than 1 at 24 h and 48 h. This is because after CAP exposure, very high death rates were observed in both MCF-7 and HME1 cells, leading to very low IC_{50} values.

The findings on the effects of CAP application in combination with NCs on HME-1 and MCF-7 cell lines indicate that NCs administered together with CAP produce a stronger and more cytotoxic effect than either CAP or NCs alone. Studies investigating the combination of CAP and NPs are quite limited in the literature, and most of these focus only on the physical carrier properties or short-term plasma effects.[55–57] For the first time in this study, both FA-targeted, dual-drug-loaded NCs—such as those incorporating CUR and/or CAPE—and magnetically directed (*in vitro*) NCs were evaluated in conjunction with CAP, resulting in the development of a versatile therapeutic system. After exposure to CAP, a rapid increase in membrane permeability occurs, which can facilitate the easier passage of NPs and drugs into the cell.[24,58,59] In this study, to increase the contact of NCs with the cell membrane, NCs were magnetophoretically forced onto the cells with a permanent magnet immediately after being applied to the cells, facilitating the penetration of NCs into the cell.[33]

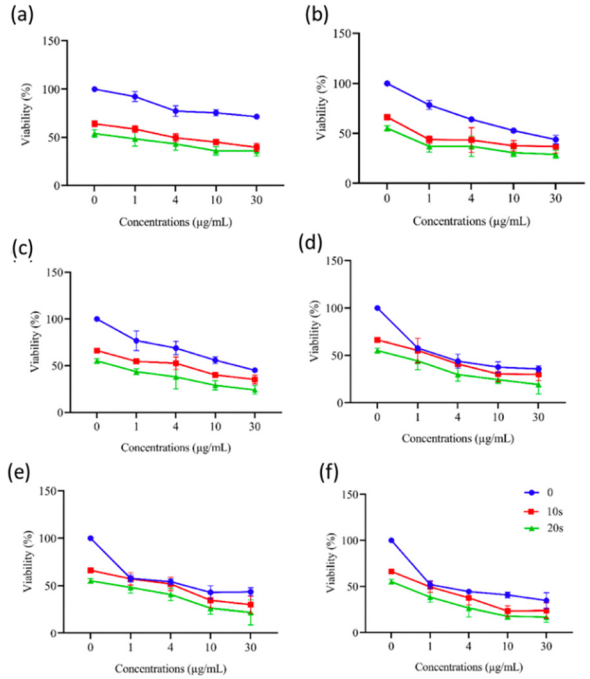

Fig. 15 Evaluation of the cytotoxicity resulting from the 48 h of co-treatment of MCF-7 cells with NCs and CAP using the MTT assay: (a) **G0**, (b) **G2**, (c) **G4**, (d) **G5**, (e) **G6**, and (f) **G7**. For sample designations, see Table 1. Statistical analysis was performed using a two-way ANOVA with multiple comparisons, where the 0 s CAP application (blue, top) was compared with the 10 s (red, middle) and 20 s (green, bottom) applications.

To evaluate synergistic and antagonistic effects, the combination index (CI) was calculated using the Chou–Talalay method.[60,61] In HME-1 cells, the combination of 1, 4, or 10 μg mL^{-1} **G7** with 10 s or 20 s CAP exposure resulted in antagonistic interactions (CI > 1). However, the combination of 20 s CAP with 30 μg mL^{-1} **G7** resulted in CI < 1, indicating a synergistic effect after 24 h of incubation, as shown in Table S9. The combination of 10 s or 20 s CAP with 1 μg mL^{-1} **G7** produced synergistic effects (CI < 1). In contrast, combinations of CAP (10 s or 20 s) with higher **G7** concentrations (4, 10, and 30 μg mL^{-1}) showed antagonistic interactions (CI > 1) after 48 h of incubation, as shown in Table S10.

Over the concentration range of 1–30 μg mL^{-1}, the combination of 10-s CAP with **G7** consistently produced CI values below 1, indicating synergy, with the strongest effect observed at 4–10 μg mL^{-1}. For the 20 s CAP combination, treatment with 1 μg mL^{-1} **G7** produced a borderline additive response (CI ≈ 1) with high variability ranging from synergy to antagonism. In contrast, combinations with 4–10 μg mL^{-1} **G7** showed a consistent synergistic effect (CI ≈ 0.5–0.6, low variability), while 30 μg mL^{-1} resulted in CI < 1, indicating synergy, but less pronounced than with mid-range doses in Table S11. After 48 h of incubation in MCF-7 cells, all mean CI values were greater than 1, indicating antagonistic interactions between **G7** NCs and CAP at all concentrations tested, as shown in Table S12.

The most significant synergistic effect was observed with the combination of 20 s of CAP exposure followed by 48 h of incubation. Under this condition, the concentration of the **G7** system at which the IC_{50} value dropped for HME-1 cells was 0.06 ± 0.08 μg mL^{-1} and that for MCF-7 cells was ± 0.06 μg mL^{-1}. These findings indicate that the potent cytotoxic effect of the dual-drug combination was further enhanced over time. Under the same conditions, even in the unmodified SPIONC structure **G0**, the IC_{50} decreased to 20.32 ± 3.06 μg mL^{-1} for HME-1 and 0.61 ± 0.07 μg mL^{-1} for MCF-7 cells, which demonstrates that CAP is an effective trigger even in bare systems. Following 20 s of CAP exposure, the SI value of CUR-CAPE-loaded NCs (**G7**) was 83.75 at 24 h, indicating a highly selective effect of the combination therapy at this dose. However, at 48 h, the SI value dropped below 1. This result is attributed to the high levels of cell death observed in both MCF-7 and HME1 cells after CAP treatment, leading to significantly lower IC_{50} values for both the cell lines.

The findings demonstrated that CAP exhibits enhanced cytotoxicity not only through direct ROS-induced effects but also *via* its interaction with NCs. Previous studies have reported that CUR and CAPE molecules promote apoptosis by down regulating the expression of certain proteins (such as HSP90AB1 and SMARCC1), activating caspase-3 and caspase-8, increasing ROS levels, and triggering multiple signalling pathways.[62–65] In this study, the synergistic effect of CUR- and CAPE-loaded NCs combined with CAP treatment appears to have led to cell death through ROS generation and apoptosis.

Reactive oxygen species (ROS) analysis

Considering the cytotoxicity results, NCs containing 30 μg mL^{-1} Fe (41.5 μg mL^{-1} Fe_3O_4) and 20 s CAP treatment were selected to examine ROS levels (Fig. 16). In HME-1 cells without CAP treatment, ROS levels in the cell medium were found to be quite low in **G4**, **G5**, **G6**, and **G7** groups (Fig. 16(a)). Compared to the control, no statistically significant increase in ROS production was observed ($p > 0.999$), indicating low oxidative stress. In contrast, CAP treatment alone statistically significantly increased ROS levels ($p < 0.0001$). When CAP and **G5**, **G6**, and **G7** were used together, ROS levels were significantly increased compared to the control ($p < 0.0001$). When CAP and **G4** were applied together, the ROS increase was found to be significant compared to the control, but slightly lower than the other NC groups ($p = 0.0021$). These findings indicate that ROS production in normal cells is mainly triggered by CAP application, while functionalized NCs alone do not create a significant oxidative stress. In MCF-7 cancer cells (Fig. 16(b)), **G6** application alone caused a significant ROS increase compared to the control ($p = 0.0116$). CAP alone or CAP combined with NCs (FA, CUR, CAPE, and CUR-CAPE) resulted in strong and statistically significant increases in ROS levels compared to the control group ($p < 0.0001$). Interestingly, CAP combination treatments consistently increased ROS, whereas NCs alone (**G4**, **G5**, **G6**, and **G7**) were not significantly different from the control when applied in the absence of CAP ($p > 0.05$).

In cancer cells, a key mechanism of cytotoxic effects following CAP exposure is ROS generation. Co-administration of NC and CAP resulted in a significant increase in ROS production in both MCF-7 and HME1 cell lines. While NC alone did not cause

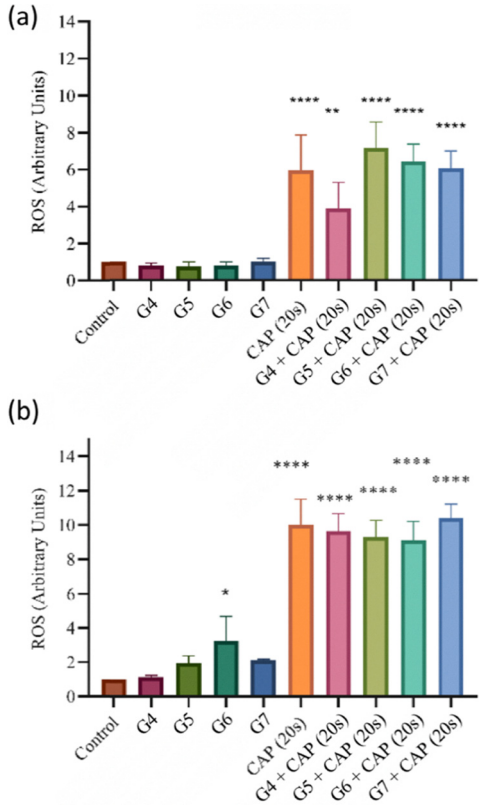

Fig. 16 (a) HME1 and (b) MCF-7 cells were exposed to 30 μg mL^{-1} NCs combined with a 20 s CAP treatment, and extracellular ROS levels were subsequently measured. For sample designations, see Table 1. Statistical analysis was performed using a one-way ANOVA with multiple comparisons.

a significant increase in ROS, co-administration with CAP resulted in significant oxidative stress. The greater increase in ROS in MCF-7 cancer cells compared to HME1 cells suggests that cancer cells act to enhance CAP-induced ROS generation. These observations are consistent with previous reports indicating that CAP can selectively increase ROS accumulation in tumour cells, resulting in DNA damage, mitochondrial dysfunction, and apoptotic or necrotic cell death pathways.[50,59] In MCF-7 cells, the combined application of MPS-SPIONCFA-CUR-CAPEs and CAP increased the average ROS level compared to the application of CAP alone, but this increase was not significant. In HME-1 cells, the combined application of **G7** (MPS-SPIONCFA) and CAP decreased the ROS level compared to the application of CAP alone. This suggests that FA has an inhibitory effect on ROS formation in normal cells.[66,67] However, it has been reported that nanomaterials loaded with redox-active compounds can increase oxidative stress responses in the tumour microenvironment.[24,55,57]

In this study, a novel core-multishell material, with a core of magnetic nanoclusters and shells of (amorphous + mesoporous) silica, was developed and loaded with active biomolecules. The synergistic effect of mesoporous silica-coated magnetic NCs functionalized with multiple drug molecules, in combination with CAP, was investigated on both normal (HME-1) and cancerous breast cell lines (MCF-7). The loading and characterization of CUR and CAPE into mesoporous silica-coated magnetic nanoclusters conjugated with folic acid have been performed for the first time in this study. This study presents four main findings. First, CUR and CAPE exhibited significantly higher release rates from nanoclusters at acidic pH values (pH 5.0 – lysosomal environment and pH 6.5 – tumour microenvironment) compared to the physiological pH 7.4. Secondly, NCs loaded with CUR and CAPE demonstrated markedly enhanced cytotoxicity compared to the unloaded NCs. This effect was significantly more pronounced in MCF-7 breast cancer cells than in HME-1 normal epithelial cells. Thirdly, the combined application of CAP and NCs, CUR, and CAPE-loaded NCs caused high toxicity in MCF-7 cells even at low concentrations. Finally, the increase in ROS levels induced by CAP was observed to play a significant role in cytotoxicity; moreover, CUR and CAPE were found to contribute to this effect not only by enhancing ROS generation but also potentially through additional biochemical pathways. According to recent studies, while plasma alone is cytotoxic, its combination with nanocarriers can provide a greater selectivity, more controlled efficacy, and increased therapeutic synergy.[57,68] In our NC system, the nanocarrier transcends the effects of plasma itself, providing dual magnetic and FA receptor-mediated targeting, and pH-sensitive, localized drug delivery ensures that the drug is activated only within the intracellular environment. Thus, CAP demonstrates that it can act more selectively and in a more controlled manner within cells where drug-loaded nanoclusters are concentrated, rather than as a cytotoxic agent dispersed throughout the environment.

Apoptosis and necrosis after combined treatment with CAP and nanoclusters

Flow cytometry analysis for HME-1 and MCF-7 cells was performed and results are presented in Fig. S6 and S7, respectively. According to flow cytometry analysis, as a result of synergistic application of **G4** and CAP in HME-1 cells, the viability was found to be 99.70%, early apoptosis was 0.14%, late apoptosis/necrosis was 0.13%, and necrosis was 0.03%, as displayed in Fig. S6(a). After **G5** and CAP application, the viability was found to be 95.90%, early apoptosis was 2.59%, late apoptosis/necrosis was 0.37% and necrosis was 1.14%, as presented in Fig. S6(b). **G6** and CAP application demonstrated 93.49% viability, 3.51% early apoptosis, 1.49% late apoptosis/necrosis and 1.51% necrosis, as shown in Fig. S6 (c). Following **G7** and CAP application, viability was found to be 80.63%, early apoptosis was 7.91%, late apoptosis/necrosis was 8.72% and necrosis was 2.74%, as presented in Fig. S6(d).

According to flow cytometry analysis in Fig. S7(a), as a result of synergistic application of **G4** and CAP in MCF7 cells, the viability was found to be 80.94%, early apoptosis was 5.53%, late apoptosis/necrosis was 3.04%, and necrosis was 10.49%. After **G5** and CAP application, the viability was found to be 66.82%, early apoptosis was 7.68%, late apoptosis/necrosis was 7.53% and necrosis was 17.97%, as shown in Fig. S7(b). **G6** and CAP application demonstrated 50.84% viability, 12.83% early apoptosis, 7.68% late apoptosis/necrosis and 28.64%. necrosis,

as presented in Fig. S6(c). Following **G7** and CAP application, the viability was found to be 71.00%, early apoptosis was 14.75%, late apoptosis/necrosis was 4.82% and necrosis was 9.44%, as displayed in Fig. S6(d).

The combination of CAP and iron oxide NCs significantly reduces cell viability and downregulates BAX/BCL-2 expression, leading the breast cancer cells to apoptosis.[69] The combination of CAP and iron oxide NCs inhibited EGFR and pERK/pAKT signalling, leading to cell apoptosis in lung cancer cells.[70] In our study, when CUR was loaded into NPs, the IC_{50} value of CUR concentration was found to be 10 ± 2 μM and 2.81 ± 0.4 μM at 24 h and 48 h, respectively, while this value was not reached with CUR alone, even at the highest concentration of 12.2 μM (equivalent to 4.5 μg mL^{-1}), as shown in Fig. S5(a). In CUR cytotoxicity in other breast cancer cell lines, the IC_{50} concentrations for MDA-MB-231 were 28.7, 22.6, and 20.1 μM after 24 h, 48 h, and 72 h, respectively. On the other hand, 12.87, 7.83, and 8.22 μM were reported in MDA-MB-468 cells after 24 h, 48 h, and 72 h of incubation, respectively.[71] Another study showed cytotoxicity for curcumin, B(Cur)2 (boron–curcumin) and Fe(Cur)3 (iron–curcumin) complexes with IC_{50} values of 25, 35 and 8 μM, respectively.[72] In our NP system with CUR loading, the IC_{50} is reached at a much lower concentration, showing the synergistic effect and therapeutic potential of the designed NPs.

Conclusions

In this study, a new generation of functional nanocarrier systems developed by coating magnetic cores with mesoporous silica shells was successfully synthesized and characterized for their dual drug carrying properties, and their synergistic effect with cold atmospheric plasma (CAP) was investigated. In particular, two different anticancer agents, curcumin (CUR) and capecitabine (CAPE), were co-loaded onto folic acid functionalized mesoporous silica coated magnetic nanoclusters for the first time. These nanocarriers exhibited superparamagnetic properties aimed to interact synergistically with CAP and were analysed in detail by a library of characterization techniques, including DLS, zeta potential, FTIR, HR-TEM, SEM-EDX, VSM, and nitrogen adsorption–desorption analyses, to understand their structural, morphological, surface, and magnetic properties in detail. When the drug release profiles of the nanocarriers were examined, it was determined that they showed significantly higher release rates under acidic conditions mimicking both the lysosomal environment (pH 5.0) and the tumour microenvironment (pH 6.5) compared to physiological pH (pH 7.4). This indicates the pH-sensitive, controlled release capability of the system. In cell-based *in vitro* experiments, nanoclusters loaded with CUR and CAPE exhibited significant cytotoxicity, especially in MCF-7 breast cancer cells compared to unloaded controls. At the same time, more limited toxicity was observed in HME-1 normal epithelial cells, supporting the selective anticancer activity potential of the developed system. Another important aspect of the study is the synergistic therapeutic effect that emerged when the developed dual drug-loaded nanocarriers were combined with CAP. This combination showed that CUR/CAPE-loaded nanoclusters caused high levels of cell death in MCF-7 cells even at low concentrations. Mechanistic analyses revealed that the increase in reactive oxygen species (ROS) levels induced by CAP underlies this effect. Furthermore, it was concluded that CUR and CAPE increase ROS production in this process and probably act at the cellular level through additional molecular pathways. The results demonstrate that this innovative nanoplatform, which is dual drug-loaded, pH-sensitive, and can be integrated with CAP, has strong potential in terms of both high efficacy and selectivity in the treatment of breast cancer. The developed system significantly increases treatment effectiveness when used in conjunction with physical therapy approaches such as CAP, while allowing for the simultaneous and targeted administration of multiple drugs. Overall, the findings highlight the promising potential of this dual-drug nanoplatform in combination with CAP as a selective and effective therapeutic strategy for breast cancer treatment.

Author contributions

Demet Erdag: conceptualization, investigation, formal analysis, methodology, writing – original draft, and writing – review and editing. M. Dolores Garrido: investigation, methodology, and writing – review and editing. Harun Basoglu and Idris Yazgan: investigation, formal analysis, methodology, and writing – review and editing. Pedro Amorós: conceptualization, project administration, supervision, validation, funding acquisition, and writing – review and editing. Leman Yalcintepe: project administration, supervision, validation, funding acquisition, and writing – review and editing. Muhammet S. Toprak: conceptualization, project administration, supervision, validation, funding acquisition, writing – original draft, and writing – review and editing.

Conflicts of interest

There are no conflicts of interest to declare.

Data availability

The data supporting this article have been included as part of the manuscript and its Supplementary Information (SI). The following are available in the Supplementary Information: **Figure S1**. The cold atmospheric plasma (CAP) source and CAP application set-up. **Figure S2**. The FT-IR spectra of the samples at various process steps: (a) Full range (600–4000 cm^{-1}), (b) 1400–600 cm^{-1}, (c) 1700–1400 cm^{-1}, and (d) 4000–2700 cm^{-1}. Sample details are presented in Table 1. **Figure S3**. STEM micrographs of SPIONCFA-CUR. **Supplementary Table 1**. Observed FT-IR bands along with their assignments for SPIONCs after various process steps. For sample designations see Table 1S. **Supplementary Table 2**. IC_{50} values

(in μg/mL) of CAP in MCF-7 cells. **Supplementary Table 3**. IC_{50} values (in μg/mL) of NCs in HME-1 cells. **Supplementary Table 4**. IC_{50} values (in μg/mL) of NCs in MCF-7 cells. **Supplementary Table 5**. IC_{50} values (in μg/mL) of CAP and NCs combined in HME-1 cells at 24h. **Supplementary Table 6**. IC_{50} values (in μg/mL) of CAP and NCs combined in HME-1 cells at 48h. **Supplementary Table 7**. IC_{50} values (in μg/mL) of CAP and NCs combined in MCF-7 cells at 24h. **Supplementary Table 8**. IC_{50} values (in μg/mL) of CAP and NCs combined in MCF-7 cells at 48h. **Supplementary Table 9**. Combination Index (CI) values for the interaction of G7 (1–10 μg/mL) with 10 s or 20 s CAP exposure in HME-1 cells after 24 h incubation. **Supplementary Table 10**. Combination Index (CI) values for the interaction of G7 (1–10 μg/mL) with 10 s or 20 s CAP exposure in HME-1 cells after 48 h incubation. **Supplementary Table 11**. Combination Index (CI) values for the interaction of G7 (1–10 μg/mL) with 10 s or 20 s CAP exposure in MCF-7 cells after 24 h incubation. **Supplementary Table 12**. Combination Index (CI) values for the interaction of G7 (1–10 μg/mL) with 10 s or 20 s CAP exposure in MCF-7 cells after 48 h incubation. **Figure S4**. (a) Nitrogen adsorption–desorption isotherms, (b) Pore size/ diameter distribution of MPS-SPIONC, along with a table summarizing the important parameters obtained. **Figure S5**. Cytotoxicity effects of (a) CUR and (b) CAPE on MCF-7 cells after 24h and 48 h incubation, as determined by MTT assay. **Figure S6**. Apoptosis results of HME-1 cells. (a) Application of **G4** (FA-conjugated nanoclusters) and CAP, (b) **G5** (CUR-loaded nanoclusters) and CAP application, (c) **G6** (CAPE-loaded nanoclusters) and CAP application. (d) **G7** (CUR-CAPE loaded nanoclusters) and CAP application. **Figure S7**. Apoptosis results of MCF-7 cells. (a) Application of **G4** (FA-conjugated nanoclusters) and CAP, (b) **G5** (CUR-loaded nanoclusters) and CAP application, (c) **G6** (CAPE-loaded nanoclusters) and CAP application. (d) **G7** (CUR-CAPE loaded nanoclusters) and CAP application. See DOI: https://doi.org/10.1039/d5tb01738f.

Acknowledgements

D. E. would like to express sincere gratitude for the support provided by the TÜBİTAK-COST 222S690-2519 grant, the TÜBİTAK 2214-A International Doctoral Research Scholarship Program, which supported one year of doctoral research at the Department of Applied Physics, KTH Royal Institute of Technology, the Scientific Research Projects Coordination Unit of Istanbul University (project no: TDK-2022-39501), and the Institute of Health Sciences-Istanbul University. D. E. also thanks Dr Lars Boeckmann for his valuable advice regarding CAP applications and acknowledges the collaborative framework of COST Action CA20114 – PlasTHER. This research was also supported by the Knut and Alice Wallenberg Foundation (KAW 2016.0057) and the project PID2021-126304OB-C43 funded by MCIN/AEI/10.13039/501100011033/ and by European Regional Development Fund – A way of making Europe. We also acknowledge the AGROALNEXT program, supported by MCIN with funding from the European Union NextGenerationEU (PRTR-C17.I1) and by Generalitat Valenciana grant number EUAGROALNEXT/2022/065. M. D. G. thanks the University of Valencia for a pre-doctoral fellowship from the program ''Atracció de Talent'' (UV-INV_PREDOC21-1914738) and acknowledges the economic support received for research stays abroad associated with it. I. Y. acknowledges the TÜBİTAK 2219 International Postdoctoral Research Program for Turkish Citizens (grant number: 1059B192200472).

Notes and references

1 H. Sung, J. Ferlay, R. L. Siegel, M. Laversanne and I. Soerjomataram, *et al.*, *Ca-Cancer J. Clin.*, 2021, **71**, 209–249.
2 A. M. Sharafaddini, K. K. Esfahani and N. Mansouri, *Multim. Tools Appl.*, 2024, **84**(21), 24079–24190.
3 R. Lapusan, R. Borlan and M. Focsan, *Nanoscale Adv.*, 2024, **6**, 2234–2259.
4 C. F. G. C. Geraldes, *Molecules*, 2024, **29**, 5591.
5 T. T. Truong, S. Mondal, V. H. M. Doan, S. Tak and J. Choi, *et al.*, *Adv. Colloid Interface Sci.*, 2024, **332**, 103263.
6 A. K. Soni and R. K. Jha, *Cureus*, 2024, **16**(4), e59234.
7 M. Xie, F. Meng, P. Wang, A. Díaz-García and M. Parkhats, *et al.*, *Int. J. Nanomed.*, 2024, **19**, 8437–8461.
8 W. Graham, M. Torbett-Dougherty, A. Islam, S. Soleimani and T. A. Bruce-Tagoe, *et al.*, *Nanomaterials*, 2025, **15**, 285.
9 A. Kumar, S. Shahvej, P. Yadav, U. Modi and A. K. Yadav, *et al.*, *Pharmaceutics*, 2025, **17**, 379.
10 G. M. Saladino, R. Kakadiya, S. R. Ansari, A. Teleki and M. S. Toprak, *Nanoscale Adv.*, 2023, **5**, 1323–1330.
11 D. Zhi, T. Yang, J. Yang, S. Fu and S. Zhang, *Acta Biomater.*, 2020, **102**, 13–34.
12 A. Angelopoulou, A. Kolokithas-Ntoukas, C. Fytas and K. Avgoustakis, *ACS Omega*, 2019, **4**, 22214–22227.
13 L. S. F. Boogerd, M. C. Boonstra, A.-J. Beck, A. Charehbili and C. E. S. Hoogstins, *et al.*, *Oncotarget*, 2016, **7**, 17442–17454.
14 R. Muralidharan, A. Babu, N. Amreddy, K. Basalingappa and M. Mehta, *et al.*, *J. Nanobiotechnol.*, 2016, **14**, 47.
15 M. Ahmadi, C. A. Ritter, T. Von Woedtke, S. Bekeschus and K. Wende, *Chem. Sci.*, 2024, **15**, 1966–2006.
16 S. Hu, Y. Xu, L. Meng, L. Huang and H. Sun, *Exp. Ther. Med.*, 2018, **16**(2), 1266–1272, DOI: 10.3892/etm.2018.6345.
17 B. Mishra, A. S. Yadav, D. Malhotra, T. Mitra and S. Sinsinwar, *et al.*, *Nanomaterials*, 2024, **14**, 1294.
18 S. Shankar, *Am. J. Biomed. Res.*, 2024, 794–805.
19 A. A. Aldeen Majeed, A. Salih Sahib, H. Shakir Mahmood, K. Kadhim Mohsin and R. Fadhl Abbas, *Asian Pac. J. Cancer Prev.*, 2023, **24**, 4219–4225.
20 O. Hahn, T. O. Waheed, K. Sridharan, T. Huemerlehner and S. Staehlke, *et al.*, *Int. J. Mater. Sci.*, 2024, **25**, 4944.
21 C. Almeida-Ferreira, R. Silva-Teixeira, A. C. Gonçalves, C. M. Marto and A. B. Sarmento-Ribeiro, *et al.*, *Int. J. Mater. Sci.*, 2022, **23**, 1698.

22 L. Boeckmann, J. Berner, M. Kordt, E. Lenz and M. Schäfer, *et al.*, *J. Adv. Res.*, 2024, **57**, 181–196.
23 S. Arndt, E. Wacker, Y.-F. Li, T. Shimizu and H. M. Thomas, *et al.*, *Exp. Dermatol.*, 2013, **22**, 284–289.
24 S. Gunes, Z. He, D. Van Acken, R. Malone and P. J. Cullen, *et al.*, *Nanomedicine*, 2021, **36**, 102436.
25 M. D. Garrido, B. Hamawandi, J. F. Serrano-Claumarchirant, G. M. Saladino and A. B. Ergül, *et al.*, *Nanoscale*, 2025, **17**, 6539–6549.
26 M. D. Garrido, M. Benítez, J. V. Ros-Lis and P. Amorós, *Nano Select*, 2024, **5**, 2300169.
27 A. D. Tripathi, Y. Labh, S. Katiyar, A. K. Singh and V. K. Chaturvedi, *et al.*, *ACS Appl. Bio Mater.*, 2024, acsabm.4c00019.
28 M. Ramezani Farani, M. Azarian, H. Heydari Sheikh Hossein, Z. Abdolvahabi and Z. Mohammadi Abgarmi, *et al.*, *ACS Appl. Bio Mater.*, 2022, **5**, 1305–1318.
29 L. Yalcintepe, D. Erdag, F. Akbas and B. Kucukkaya, *Clin. Exp. Pharmacol. Physiol.*, 2020, **47**, 1221–1230.
30 Y. H. Lim, C. W. Oo, R. Y. Koh, G. L. Voon and M. Y. Yew, *et al.*, *Drug Dev. Res.*, 2020, **81**, 994–1003.
31 C. H. Wong, B. Khor, V. Murugaiyah, N. J. Chear and W. Yam, *Drug Dev. Res.*, 2025, **86**, e70100.
32 T. Tronina, A. Bartmańska, J. Popłoński, M. Rychlicka and S. Sordon, *et al.*, *Int. J. Mater. Sci.*, 2023, **24**, 7408.
33 H. Basoglu, B. Goncu and F. Akbas, *Cancer Gene Ther.*, 2018, **25**, 141–147.
34 S. Badragheh, M. Zeeb and M. R. Talei Bavil Olyai, *RSC Adv.*, 2018, **8**, 30550–30561.
35 Y.-S. Li, J. S. Church, A. L. Woodhead and F. Moussa, *Spectrochim. Acta, Part A*, 2010, **76**, 484–489.
36 K. Reczyńska, M. Marszałek, A. Zarzycki, W. Reczyński and K. Kornaus, *et al.*, *Nanomaterials*, 2020, **10**, 1076.
37 H. Ameli and N. Alizadeh, *RSC Adv.*, 2022, **12**, 4681–4691.
38 Z. Guo, T. He, Y. Lou, G. Xu and Q. Jia, *et al.*, *Science*, 2025, **9**, 421.
39 K. AbouAitah, A. Swiderska-Sroda, A. A. Farghali, J. Wojnarowicz and A. Stefanek, *et al.*, *Oncotarget*, 2018, **9**, 26466–26490.
40 S. Shome, A. D. Talukdar, S. Tewari, S. Choudhury and M. K. Bhattacharya, *et al.*, *Biotechnol. Appl. Biochem.*, 2021, **68**, 603–615.
41 M. A. Raja, M. Maldonado, J. Chen, Y. Zhong and J. Gu, *Int. J. Nanomed.*, 2021, **16**, 6231–6247.
42 N. Ye, P. Zhao, S. Ayue, S. Qi and Y. Ye, *et al.*, *Int. J. Biol. Macromol.*, 2023, **232**, 123229.
43 W. Hong, F. Guo, N. Yu, S. Ying and B. Lou, *et al.*, *Drug Des., Dev. Ther.*, 2021, **15**, 2843–2855.
44 M. T. Luiz, J. A. P. Dutra, T. D. C. Ribeiro, G. C. Carvalho and R. M. Sábio, *et al.*, *Colloids Surf., A*, 2022, **645**, 128935.
45 M. Bernabé-Pineda, M. T. Ramírez-Silva, M. Romero-Romo, E. González-Vergara and A. Rojas-Hernández, *Spectrochim. Acta, Part A*, 2004, **60**, 1091–1097.
46 Z. Wang, M. H. M. Leung, T. W. Kee and D. S. English, *Langmuir*, 2010, **26**, 5520–5526.
47 S. C. Gupta, S. Prasad, J. H. Kim, S. Patchva and L. J. Webb, *et al.*, *Nat. Prod. Rep.*, 2011, **28**, 1937.
48 S. Zhang, H. Yang, L. Zhao, R. Gan and P. Tang, *et al.*, *J. Biomol. Struct. Dyn.*, 2019, **37**, 1451–1463.
49 M. L. Semmler, S. Bekeschus, M. Schäfer, T. Bernhardt and T. Fischer, *et al.*, *Cancers*, 2020, **12**, 269.
50 S. J. Kim and T. H. Chung, *Sci. Rep.*, 2016, **6**, 20332.
51 M. Keidar, A. Shashurin, O. Volotskova, M. Ann Stepp and P. Srinivasan, *et al.*, *Phys. Plasmas*, 2013, **20**, 057101.
52 H.-R. Metelmann, D. S. Nedrelow, C. Seebauer, M. Schuster and T. Von Woedtke, *et al.*, *Clin. Plasma Med.*, 2015, **3**, 17–23.
53 H.-R. Metelmann, C. Seebauer, V. Miller, A. Fridman and G. Bauer, *et al.*, *Clin. Plasma Med.*, 2018, **9**, 6–13.
54 T. Fang, Z. Chen and G. Chen, *Bioact. Mater.*, 2025, **53**, 433–458.
55 Z. Yazdani, P. Biparva, A. Rafiei, M. Kardan and S. Hadavi, *PLoS One*, 2024, **19**, e0304502.
56 X. Cao, M. Chen, T. Fang, Y. Deng and L. Wang, *et al.*, *J. Nanobiotechnol.*, 2025, **23**, 136.
57 X. Dai, Y. Dai, Y. Zheng and Y. Lv, *RSC Adv.*, 2024, **14**, 29039–29051.
58 M. Gelker, C. C. Müller-Goymann and W. Viöl, *Skin Pharmacol. Physiol.*, 2020, **33**, 69–76.
59 B. Yadav and M. S. Roopesh, *Microorganisms*, 2023, **11**, 682.
60 D. R. Abu Alsamen, Z. Z. Zakaraya, A. Abed, A. A. Alsa'd and M. R. Alnajdawi, *PLoS One*, 2025, **20**, e0334427.
61 S. Oncu, M. Becit-Kizilkaya, S. Sen, A. B. Ugur-Kaplan and M. Cetin, *et al.*, *Naunyn-Schmiedeberg's Arch. Pharmacol.*, 2024, **397**, 4871–4881.
62 S. Zhang, S. Fan, Z. Wang, W. Hou and T. S. Liu, *et al.*, *Oxid. Med. Cell. Longevity*, 2022, **2022**, 1–15.
63 S. Zhang, Z. Wang, S. Fan, T. Liu and S. Yoshida, *et al.*, *Front. Immunol.*, 2021, **12**, 737849.
64 S. Kuttikrishnan, K. S. Siveen, K. S. Prabhu, A. Q. Khan and E. I. Ahmed, *et al.*, *Oncology*, 2019, **9**, 484.
65 P. Anand, C. Sundaram, S. Jhurani, A. B. Kunnumakkara and B. B. Aggarwal, *Cancer Lett.*, 2008, **267**, 133–164.
66 F. Cheng, J. Lan, W. Xia, C. Tu and B. Chen, *et al.*, *Cell Biochem. Biophys.*, 2016, **74**, 205–211.
67 N. Li, L. Wen, Z. Yu, T. Li and T. Wang, *et al.*, *Nutrition*, 2022, **9**, 1035162.
68 A. Moghaddasfar, G. Mohammadi Ziarani, R. Luque and A. Badiei, *Mater. Adv.*, 2025, **6**, 3416–3432.
69 S. Irani, R. Mirfakhraie and A. Jalili, *OncoTargets Ther.*, 2016, **9**, 5911–5917.
70 W. Li, H. Yu, D. Ding, Z. Chen and Y. Wang, *et al.*, *Free Radicals Biol. Med.*, 2019, **130**, 71–81.
71 M. Li, T. Guo, J. Lin, X. Huang and Q. Ke, *et al.*, *J. Ethnopharmacol.*, 2022, **283**, 114689.
72 F. Mohammed, F. Rashid-Doubell, S. Taha, S. Cassidy and S. Fredericks, *Int. J. Oncol.*, 2020, **57**, 445–455.

